Eur. J. Mineral., 34, 469–491, 2022
https://doi.org/10.5194/ejm-34-469-2022

European Journal of Mineralogy
Open Access

A snapshot of the transition from monogenetic volcanoes to composite volcanoes: case study on the Wulanhada Volcanic Field (northern China)

Diao Luo[1], Marc K. Reichow[2], Tong Hou[1,3], M. Santosh[1,4], Zhaochong Zhang[1], Meng Wang[1], Jingyi Qin[1], Daoming Yang[1], Ronghao Pan[1], Xudong Wang[1], François Holtz[3], and Roman Botcharnikov[5]

[1]State Key Laboratory of Geological Processes and Mineral Resources, China University of Geosciences, Beijing 100083, China
[2]School of Geography, Geology and the Environment (SGGE), University of Leicester, Leicester, LE1 7RH, UK
[3]Institute of Mineralogy, Leibniz Universität Hannover, Callinstr. 3, 30167 Hanover, Germany
[4]Department of Earth Sciences, University of Adelaide, Adelaide, SA 5005, Australia
[5]Institut für Geowissenschaften, Johannes Gutenberg-Universität Mainz, J.-J.-Becherweg 21, 55128, Mainz, Germany

Correspondence: Tong Hou (thou@cugb.edu.cn)

Received: 14 March 2022 – Revised: 19 September 2022 – Accepted: 24 September 2022 – Published: 20 October 2022

Abstract. The transition processes from monogenetic volcanoes to composite volcanoes are poorly understood. The Late Pleistocene to Holocene intraplate monogenetic Wulanhada Volcanic Field (WVF) in northern China provides a snapshot of such a transition. Here we present petrographic observations, mineral chemistry, bulk rock major and trace element data, thermobarometry, and a partial melting model for the WVF to evaluate the lithology and partial melting degree of the mantle source, the crystallization conditions, and pre-eruptive magmatic processes occurring within the magma plumbing system. The far-field effect of India–Eurasia collision resulted in a relatively high degree (10 %–20 %) of partial melting of a carbonate-bearing eclogite (∼ 3 wt % carbonate; Gt/Cpx ≈ 2 : 8, where Gt denotes garnet and Cpx denotes clinopyroxene) followed by interaction with ambient peridotite. The primary melts ascended to the depth of the Moho (∼ 33–36 km depth), crystallized olivine, clinopyroxene and plagioclase at the temperature of 1100–1160 °C with the melt water contents of 1.1 wt %–2.3 wt %. Part of the primary melt interacted with the lithospheric mantle during ascent, resulting in an increase in the MgO contents and a decrease in the alkaline contents. The modified magma was subsequently directly emplaced into the middle crust (∼ 23–26 km depth) and crystallized olivine, clinopyroxene and plagioclase at the temperature of 1100–1160 °C. The primary melts from the same mantle sources migrated upward to the two-level magma reservoirs to form minerals with complex textures (including reverse and oscillatory zoning and sieve texture). Magma erupted along the NE–SW-striking basement fault and the NW–SE-striking Wulanhada–Gaowusu fault in response to the combined effects of regional tectonic stress and magma replenishment. The crustal magma reservoir in the WVF may represent a snapshot of the transition from monogenetic volcanoes to composite volcanoes. It is possible to form a composite volcano with large magma volumes and complex compositions if the magma is continuously supplied from the source and experiences assimilation and fractional crystallization processes in the magma plumbing system at crustal depth.

Published by Copernicus Publications on behalf of the European mineralogical societies DMG, SEM, SIMP & SFMC.

1 Introduction

Monogenetic eruptions are one of the most widespread forms of volcanism on Earth, with polygenetic volcanism occurring in intraplate, extensional and subduction-related settings (e.g., Hildreth, 2007; Cañón-Tapia, 2016). Although the eruption lifespan of a single monogenetic volcano is usually short and eruptive volumes are small ($< 1\,km^3$), they often form part of much larger structures including multiple monogenetic volcanoes known as a volcanic field. These monogenetic volcanic fields are clusters of scattered, volcanic centers (e.g., Walker, 1993; Németh and Kereszturi, 2015; Re et al., 2017) that tend to occur as spatter cones, scoria or cinder cones, tuff and tephra rings, maar craters, tuff cones, and a few small shield volcanoes (e.g., Martin and Németh, 2006; Valentine et al., 2006; Valentine and Gregg, 2008; Coote et al., 2018).

The small eruptive volumes and entrainment of mantle xenoliths in monogenetic volcanic fields are generally assumed to have not undergone significant modification during the magmatic evolution processes (such as crustal contamination and fractional crystallization or magma recharge) on ascent from source to surface (e.g., McGee and Smith, 2016; Smith and Németh, 2017; Brenna et al., 2018). This is different from polygenetic volcanism, in which magmatic evolution occurs in interconnected magma reservoirs that are repeatedly replenished and erupt from a stable central conduit system, building a large composite edifice consisting of the products of eruptions with conical morphology (e.g., Cañón-Tapia and Walker, 2004; Devine et al., 2003; Watanabe et al., 2006; Zellmer and Annen, 2008). A consequence of these systematic differences is that monogenetic eruptions produce low cumulative volumes of commonly primitive compositions, whereas polygenetic volcanoes generate large volumes and evolved magmas (e.g., Lynch et al., 1993; Wei et al., 2007; Blondes et al., 2008; Brenna et al., 2012).

Both composite and monogenetic volcanoes are observed to coexist in the same volcanic field (e.g., Lynch et al., 1993; Wei et al., 2007; McLeod et al., 2022) and can be divided into two styles based on their field and genetic relationship. One is that the compositions of monogenetic volcanoes are controlled by composite volcanoes. Monogenetic cones on the flanks of stratovolcanoes are generally regarded as parasitic vents connected to the magma plumbing system of the main volcano (Wilson and Head, 1988; Ablay et al., 1998; Corazzato and Tibaldi, 2006). Another style is that the composite volcanoes and monogenetic volcanoes erupted and evolved independently. For example, Santa Clara, a composite volcano in the Pinacate Volcanic Field, Mexico, is considered to be unrelated to the dispersed monogenetic volcanoes (Lynch et al., 1993). Currently, the evolution processes from monogenetic volcanoes to composite volcanoes with a wide range of compositions are poorly understood (Brenna et al., 2012).

The Late Pleistocene to Holocene monogenetic Wulanhada Volcanic Field (WVF) is one of the Cenozoic monogenetic intraplate volcanic fields in northeast China and is located at the boundary between the northwestern margin of the North China Craton and the southern margin of the Daxing'anling–Mongolia Orogenic Belt (Fig. 1; Fan et al., 2014). The volcanic cones in the WVF are linearly distributed along the NE–SW-striking basement faults and the NW–SE-striking Wulanhada–Gaowusu fault (W–G fault) system. The WVF has been interpreted to be derived from the partial melting of carbonated peridotite in the proportion of 4 %–5 % based on bulk rock trace element and Sr–Nd–Pb–Hf–Mg isotopic compositions (e.g., Fan et al., 2014; Zhao et al., 2019; Sun et al., 2021). However, magma processes (such as fractional crystallization or potential magma mixing) that occurred in the source and magma plumbing system have not been well constrained. In this study, we (1) place constraints upon the lithology of the mantle source, the degree of partial melting and the interaction with the mantle and (2) evaluate the pre-eruptive crystallization conditions and magmatic processes occurring within the magma plumbing system based on comprehensive studies of high-resolution mineralogy, petrography, bulk rock major and trace element geochemistry, and thermobarometric and hygrometric calculation. Our study on the Wulanhada Volcanic Field represents a snapshot of the transition from monogenetic volcanoes to composite volcanoes, which has significance for the evolution of intraplate monogenetic volcanism.

2 Geological and volcanological framework

Cenozoic volcanism in North China, including hundreds of individual volcanoes, is spread over an area of $\sim 50\,000\,km^2$ and associated with two north–south-trending parallel geological lineaments, i.e., the Daxing'anling–Taihangshan gravity lineament (DTGL) and Tan–Lu fault zone that divide east China from west China (Zhao et al., 2019). The late-Cenozoic Nuomin, Halaha, Dalinor, Abaga, Wulanhada and Datong monogenetic volcanic fields formed from north to south along the DTGL (Fig. 1a). The Wulanhada Volcanic Field (WVF) is located between the northwestern margin of the North China Craton and the southern margin of the Daxing'anling–Mongolia Orogenic Belt. The study area has experienced the amalgamation of the crustal blocks within the North China Craton at $\sim 1.8\,Ga$ (Fig. 1b; Zhao et al., 2001), the closure of the Paleo-Asian Ocean and the Mongol–Okhotsk Ocean during the Mesozoic (Sengor and Natalin, 1996; Maruyama, 1997; Li, 2006; Xu et al., 2013), and the westward subduction of the Pacific slab beneath eastern China since the Early or Late Cretaceous (Niu, 2005). Seismic tomography had revealed that the WVF was above the front edge of the subducted Pacific slab (Huang and Zhao, 2006; Wei et al., 2012; Liu et al., 2017), and volcanism is generally considered to be associated with the subduction of the Pacific slab (Fan et al., 2014).

The basement of the WVF is primarily composed of Proterozoic quartzite, marble schist and gneiss in the north of the province, whereas granites of same age dominate the central and southern area (Bai et al., 2008). The WVF hosts 30 small monogenetic volcanic edifices including scoria cones, lava shields, spatter cones and lavas covering an area of 180 km^2. Nearly all eruptive vents are distributed around the NE–SW-striking basement faults and the NW–SE-striking Wulanhada–Gaowusu fault (W–G fault) system. The W–G fault is a major lithospheric extensional structure of the Shangdu basin (Zhao et al., 2019), which formed from the late stage of Lüliang movement to the Cenozoic (Lu et al., 2002). The composition of the magmas that erupted in the WVF range from trachybasalt to tephrite, varying a little to basaltic trachyandesite, all with a sodic alkaline affinity (Fan et al., 2014; Zhao et al., 2019).

The WVF volcanic rocks are considered to have been formed from the Late Pleistocene to Holocene based on field relationships of the well-preserved volcanic edifices and supported by thermoluminescence dating on lavas overlaying the loess, which provide minimum ages of 21.05–30.56 ka (Bai et al., 2008). Recent K–Ar ages on WVF lavas representing the entire volcanic activity range between 10.8 and 0.22 Ma, indicating a slightly longer timing with a supposedly west-to-east progression of the volcanic activity (Zhao et al., 2019). There are, however, no high-precision age determinations available, and therefore the temporal evolution of volcanism in the region is not well constrained and should be the subject of future studies. We focus here on six of the 0.50 to 0.22 Ma old and well-preserved volcanic centers: Beiliandanlu (BLDL), Zhongliandanlu (ZLDL), Nanliandanlu (NLDL), Heinaobao (HNB), Huoshaoshan (HSS) and Hongshan (HS). These monogenetic volcanoes of the WVF encompass similar magmatic styles and the compositional range of the field, and the following characterization is a brief description of these volcanoes.

The Beiliandanlu volcano is a scoria cone $\sim$ 510 m in diameter, rising 91 m above the surrounding lava plains that consist of variably welded and non-welded lapilli to blocks and bombs; two associated lavas extend 700 m to the northwest covering an area of 3 km^2 and 2.5 km to the southeast covering an area of 3 km^2, having an approximate volume of 5 km^3.

The Zhongliandanlu volcano is the largest scoria cone of the WVF at $\sim$ 680 m in diameter, reaching heights of $\sim$ 81 m and containing a 30 m deep, 180 m wide crater. ZLDL comprises coarse spatter bombs and variably sized lapilli and lava extending 19 km to the southeast, covering an area of 34 km^2 with a volume of approximately 1.7 km^3.

The Nanliandanlu volcano reaches heights of $\sim$ 64 m with $\sim$ 620 m in diameter. Its outcrops display a complete volcanic sequence because of quarrying which is composed of variably sized pyroclastic deposits including volcanic ash, lapilli, block, bombs and lava, suggesting Strombolian eruptive style (Fig. 2a; Bai et al., 2008). The lava flow extends 3 km to the northwest, covering an area of 9 km^2 with a volume of approximately 0.45 km^3.

The Heinaobao volcano is located between BLDL and ZLDL and is composed of one large cone (51 m in height, 430 m in diameter) and three smaller satellite cones. The southeast flank of HNB displays volcaniclastic sequences consisting of bedded ash, lapilli layers and scoria due to artificial destruction. Their volcaniclastic sequences unconformably overlie the basement Variscan granodiorite in the WVF (Fig. 2b). In detail, there is 1–2 cm thick soil formation between eruptive units, indicating that events were non-continuous with short periods of quiescence. The lava flow extends 300 m to the northwest, covering an area of 3 km^2 with a volume of approximately 0.15 km^3.

The Hongshan volcano, located in the southeast part of the WVF, is a relatively low scoria cone reaching heights of $\sim$ 19 m with $\sim$ 110 m in diameter. HS consists of variably unconsolidated lapilli, block, bombs and short lava, extending 300 m to the southwest and covering an area of 2 km^2 with a volume of 0.1 km^3 (Fig. 2c).

The Huoshaoshan volcano is located to the northwest of HS, and their center vents are only 200 m apart, parallel to the W–G fault. HSS hosts two calderas comprising coarse spatter bombs and variably sized lapilli and lava $\sim$ 200 m long to the southwest, covering an area of 3 km^2 with a volume of 0.15 km^3 (Fig. 2d).

3 Analytical techniques and sampling

3.1 Sampling

Thirty-one lava and scoria samples of six representative volcanic edifices from the WVF were collected in July 2018, including (1) the Beiliandanlu volcano (lava – BLDL1-2, BLDL1-4, BLDL1-8, BLDL1-11; scoria – BLDL1-7, BLDL1-10), (2) the Zhongliandanlu volcano (lava – ZLDL3-1, ZLDL3-2, ZLDL3-3; scoria – ZLDL1-3, ZLDL1-6), (3) the Nanliandanlu volcano (lava – NLDL1-1, NLDL1-2, NLDL2-1; scoria –NLDL2-6, NLDL2-9), (4) the Heinanbao volcano (lava – HNB1-5, HNB-ZM; scoria – HNB1-1, HNB1-2), (5) the Huoshaoshan volcano (lava – HSS07, HSS08; scoria – HSS01, HSS02, HSS05, HSS06) and (6) the Hongshan volcano (lava – HS01-2, HS04; scoria – HS01-1, HS03, HS05). Information on sample composition and locations is shown in Table S1 in the Supplement.

3.2 Electron microprobe analysis (EMPA)

Mineral chemistry was analyzed at the Key Laboratory of Submarine Geosciences, State Oceanic Administration, Second Institute of Oceanography, Ministry of Natural Resources, China, using an electron microprobe analyzer (JXA-8100, JEOL) equipped with wavelength-dispersive X-ray spectrometers and one energy-dispersive X-ray spectrometer analyzer. For phenocrysts crystals and fine-grained matrices,

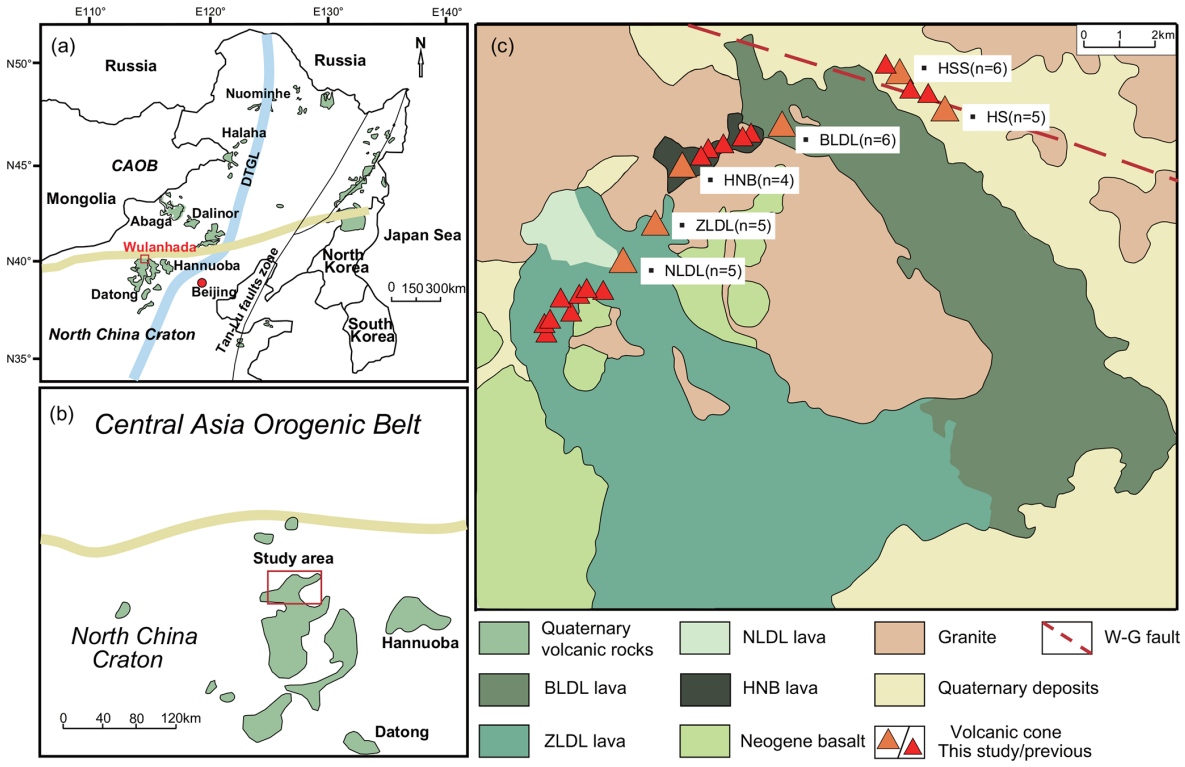

Figure 1. **(a)** Map of northeastern China showing the distribution of Cenozoic basalts and the location of the Wulanhada Volcanic Field (WVF; modified after Zhao et al., 2019). The light blue band marks the Daxing'anling–Taihangshan gravity lineament (DTGL); the yellow band shows the block boundary. CAOB refers to the Central Asian Orogenic Belt. **(b)** Schematic geological map of the WVF and adjacent area (modified from Ma, 1989). **(c)** Geological map of the WVF showing locations of Quaternary volcanoes, adapted from Bai et al. (2008) and Fan et al. (2014). W–G fault refers to the Wulanhada–Gaowusu fault. HS, Hongshan; HSS, Huoshaoshan; BLDL, Beiliandanlu; HNB, Heinaobao; ZLDL, Zhongliandanlu; NLDL, Nanliandanlu. The number of bulk rock analyses (n) for each volcano is indicated in brackets.

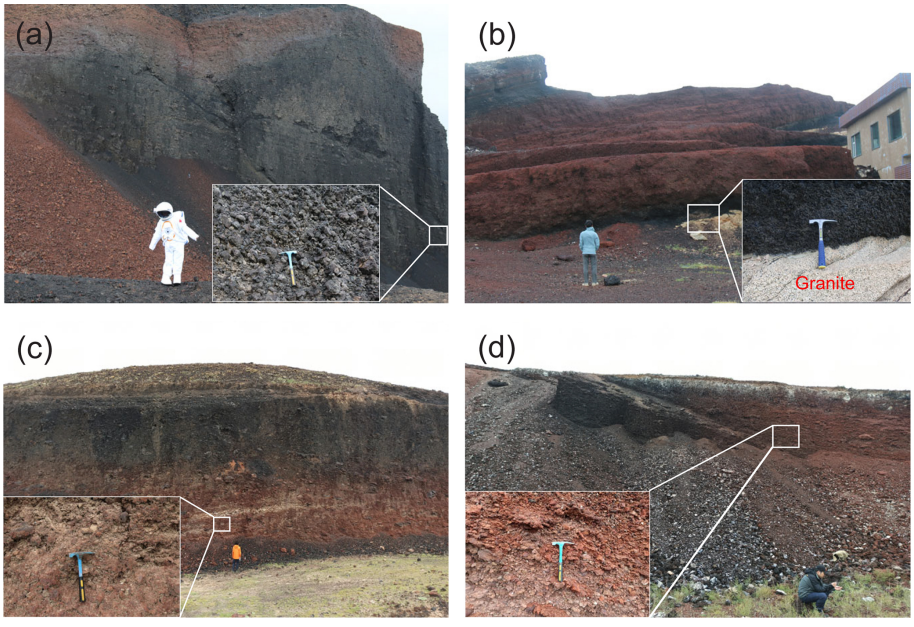

Figure 2. Field photographs of the Wulanhada Volcanic Field. **(a)** Nanliandanlu volcano and detail of scoria cone. **(b)** Heinaobao volcano and the scoria material overlays the granite. **(c)** Hongshan volcano and detail of scoria cone. **(d)** Huoshaoshan volcano and detail of scoria cone.

the instrument was operated at 15 nA, 15 kV, and a focused 1 or 5 µm beam size depending on crystal size. The analytical precision relative to standard reference samples provided by the National Technical Committee for Standardization of Microbeam Analysis (China) or produced by SPI Supplies (USA) was better than 5 % (2σ).

3.3 Bulk rock X-ray fluorescence (XRF) analysis

A total of 31 lava and scoria samples free from obvious or with only slight signs of alteration were selected and prepared for analysis. Where present, signs of alteration (slight discoloring) were removed with a saw before jaw crushing of hand specimens and the subsequent grounding of the millimeter-sized rock chips in agate mills to fine powders. Bulk rock major compositions were obtained on fusion beads by X-ray fluorescence (XRF) analysis using a PW4400 at the laboratory of Nanjing Hongchuang Geological Exploration Technology Service Co., Ltd. (NHETS), in Nanjing, China. Total loss on ignition (LOI) was measured on pre-dried powders after ignition at 950 °C in air for 1 h. Calibrations to monitor accuracy and precision for major element analysis were set using international rock reference material including W-2, BHVO-1 and AGV-1, resulting in analytical uncertainties < 1 %.

3.4 Inductively coupled plasma mass spectrometry (ICP-MS)

Trace elements were measured by inductively coupled plasma mass spectrometry (ICP-MS; PerkinElmer ELAN 300D) at NHETS. A total of 25 mg of crushed sample powders was dissolved using a 1 mL HF and 0.5 mL HNO_3 mixture (2 : 1) in a sealed Teflon bottle at 190 °C for 48 h. After cooling, the bottles were opened and then evaporated to dryness on a hot plate; the addition and evaporation of 1 mL HNO_3 were repeated twice. Finally, the residue was heated with 2 mL of distilled water and HNO_3 mixture (1 : 1) at 120 °C for 8 h and then made up to 50 mL before analyses. Precision values are calculated from the averages of repeated analysis of national standards GSR-1 and GSR-3, and the analytical deviations were lower than 10 %.

4 Results

4.1 Petrography

The proportions of phenocrysts, vesicles and groundmass were determined by point counting with a PELCON Automatic Point Counter for 30 representative samples at the China University of Geosciences (Beijing). We manually operated a mechanical slide along the x and y axes in steps of 0.3 mm, giving between 1000 and 3000 points per thin section. Phenocrysts of plagioclase, olivine, clinopyroxene, vesicles and groundmass defined here as all grains < 200 µm were counted. The mass fraction of crystals on a vesicle-free basis was calculated by considering the following densities: 3.3 g cm^{-3} for olivine, 3.2 g cm^{-3} for clinopyroxene, and 2.7 g cm^{-3} for plagioclase and groundmass. Both raw point-counting data and crystal mass fractions are shown in Table 1.

All samples from different cones of the WVF show porphyritic textures with phenocrysts of plagioclase (3 vol %–18 vol %, 0.75 to 2.5 mm long), clinopyroxene (1 vol %–5 vol %, 0.5–1.5 mm long), olivine (1 vol %–3 vol %, 0.3–1 mm long) and Fe–Ti oxides (0.5 vol %–1 vol %, 0.3–0.75 mm long) embedded in a microcrystalline groundmass consisting of the same mineral phases. Phenocrysts occur as single crystals and as glomerocrysts that are nearly ubiquitous and are commonly dominated by euhedral crystals. These phenocryst phases will be described below. Selected microphotographs are displayed in Fig. 3.

4.1.1 Olivine composition

Olivine within samples from the WVF occurs as euhedral to subhedral crystals in the glomerocrysts and phenocrysts as well as groundmass, which were generally analyzed in both the core and the rim. The compositions of olivine minerals are listed in Table S2. The Fo content (forsterite content, molar Mg/(Mg + Fe)) of olivine is clustered in the range of 72–75 except the rim of individual phenocryst and groundmass is in the range of 59–61 (Fig. 4c), which could result from last-stage crystallization or represent disequilibrium growth according to rapid cooling (Coote et al., 2019).

Backscattered electron (BSE) images of the olivine crystals from the samples in the WVF generally display normal and reverse as well as oscillatory zoning patterns. A representative of a reverse mineral profile is shown in Fig. 5h, i.e., the core of the reverse-zoned olivine span from Fo = 68 to Fo = 69 enclosed by a thin (ca. 10–20 µm) more Mg-rich region with Fo of 71–73, which may imply recharge by a more primitive magma. Over three-quarters the WVF olivine crystals show normal zoning with core-to-rim variation in Fo ranging 0.9 %–5 %.

4.1.2 Clinopyroxene composition

Clinopyroxene is pervasively present, occurring as individual phenocrysts, glomerocrysts and groundmass. The compositions of clinopyroxene are listed in Table S3. According to the classification scheme of Morimoto (1988), clinopyroxene phenocrysts and groundmass are classified as diopside–augite ($En_{33–52}Fs_{9–18}Wo_{32–51}$; Fig. 4a) with Mg# values (Mg# is molar 100 × Mg/(Mg + Fe)) varying from 66 to 84 (Fig. 4d). Four types of clinopyroxene are divided according to BSE imagery together with mineral compositional profiles: normal, reverse zoning and oscillatory zoning as well as sieve texture (Fig. 5). The distribution of mineral types of the volcanoes is shown in Table 2.

Table 1. Raw point-counting data and mass fractions for samples of the WVF.

Sample	Raw counts					Mass fraction (%)				
	Plg	Cpx	Ol	Gm	Ves	Plg	Cpx	Ol	Gm	Phenocrysts
BLDL1-2	94	26	16	1890	425	4.6	1.5	1.0	92.9	7.1
BLDL1-4	92	7	2	1861	317	4.7	0.4	0.1	94.8	5.2
BLDL1-7	38	12	26	1703	416	2.1	0.8	1.8	95.3	4.7
BLDL1-8	112	16	13	1992	231	5.2	0.9	0.7	93.1	6.9
BLDL1-10	82	19	12	1968	321	3.9	1.1	0.7	94.3	5.7
BLDL1-11	26	5	16	1934	329	1.3	0.3	1.0	97.4	2.6
ZLDL1-3	4	17	8	815	202	0.5	2.4	1.2	96.0	4.0
ZLDL1-6	12	45	15	1682	454	0.7	3.0	1.0	95.3	4.7
ZLDL3-1	372	49	41	2855	53	11.2	1.7	1.5	85.6	14.4
ZLDL3-2	398	71	3	1262	85	22.8	4.8	0.2	72.2	27.8
ZLDL3-3	36	31	15	1845	156	1.9	1.9	0.9	95.3	4.7
NLDL01-1	154	65	21	1546	220	8.5	4.3	1.4	85.8	14.2
NLDL2-1	274	131	120	1914	259	11.0	6.2	5.9	76.9	23.1
NLDL02-6	26	29	1	300	347	7.2	9.5	0.3	83.0	17.0
NLDL02-9	142	102	7	1384	337	8.6	7.3	0.5	83.6	16.4
HS01-1	282	14	19	1834	691	13.1	0.8	1.1	85.1	14.9
HS01-2	467	19	7	1797	584	20.3	1.0	0.4	78.3	21.7
HS03	256	14	30	1536	753	13.9	0.9	2.0	83.2	16.8
HS04	102	70	18	1773	508	5.2	4.2	1.1	89.5	10.5
HS05	349	23	14	1358	778	19.9	1.6	1.0	77.5	22.5
HNB1-1	150	32	16	1259	1324	10.2	2.6	1.3	85.9	14.1
HNB01-2	89	20	16	1033	908	7.6	2.0	1.7	88.6	11.4
HNB1-5	462	34	36	2077	427	17.6	1.5	1.7	79.2	20.8
HNB-ZM	342	22	50	2022	304	14.0	1.1	2.5	82.5	17.5
HSS01	509	31	41	1542	725	23.8	1.7	2.3	72.1	27.9
HSS02	266	21	8	1506	716	14.7	1.4	0.5	83.4	16.6
HSS05	176	29	9	1759	637	8.9	1.7	0.6	88.8	11.2
HSS06	146	34	10	1900	919	7.0	1.9	0.6	90.5	9.5
HSS07	227	37	33	2091	810	9.4	1.8	1.7	87.0	13.0
HSS08	173	73	33	1833	986	8.1	4.1	1.9	85.9	14.1

Abbreviations: Plg, plagioclase; Cpx, clinopyroxene; Ol, olivine; Gm, groundmass; Ves, vesicles.

1. Type 1 clinopyroxene (Cpx-1) is the common type in all studied samples, generally homogeneous or normally zoned with slightly decreasing Mg# to the rim (Fig. 5a). Mg# of Type 1 ranges from 66–84 with a peak of 75. The normally zoned clinopyroxenes are euhedral in shape in general and compositionally varied from Mg# = 77 to 73 along the core–rim profile (Fig. 5a).

2. Type 2 clinopyroxene (Cpx-2) is also observed in all the studied samples. Mg# of Type 2 ranges from 69–82 with a peak of 75. It is characterized by a euhedral core with Mg# of ∼ 69 surrounded by a narrow rim with Mg# of 75–77, indicating overgrowth in a more mafic or primitive melt (Fig. 5c).

3. Type 3 clinopyroxene (Cpx-3) crystals are characterized by oscillatory zoning without sieve texture, accounting for ∼ 15 % of the clinopyroxene population. Mg# of Type 1 ranges from 66–78 with a peak of 72. Crystals with oscillatory zoning are usually faintly defined euhedral shapes with widths ranging from ∼ 10 to 70 µm. From core to rim, the representative scenarios of oscillatory zoning generally exhibit a core with an intermediate Mg# (∼ 75) with an inner mantle with relatively low Mg# values (∼ 70), surrounded by a high Mg# value (∼ 80) outer mantle, and finally the rim with relatively low Mg# values (∼ 75) (Fig. 5e).

4. Type 4 clinopyroxene (Cpx-4) represents minor proportions (5 %) of the clinopyroxene crystal population of the samples in the WVF and is characterized by sieve-textured cores which are commonly enclosed by a compositionally homogeneous mantle/rim, occasionally displaying oscillatory zoning at the outermost rim (Fig. 5g).

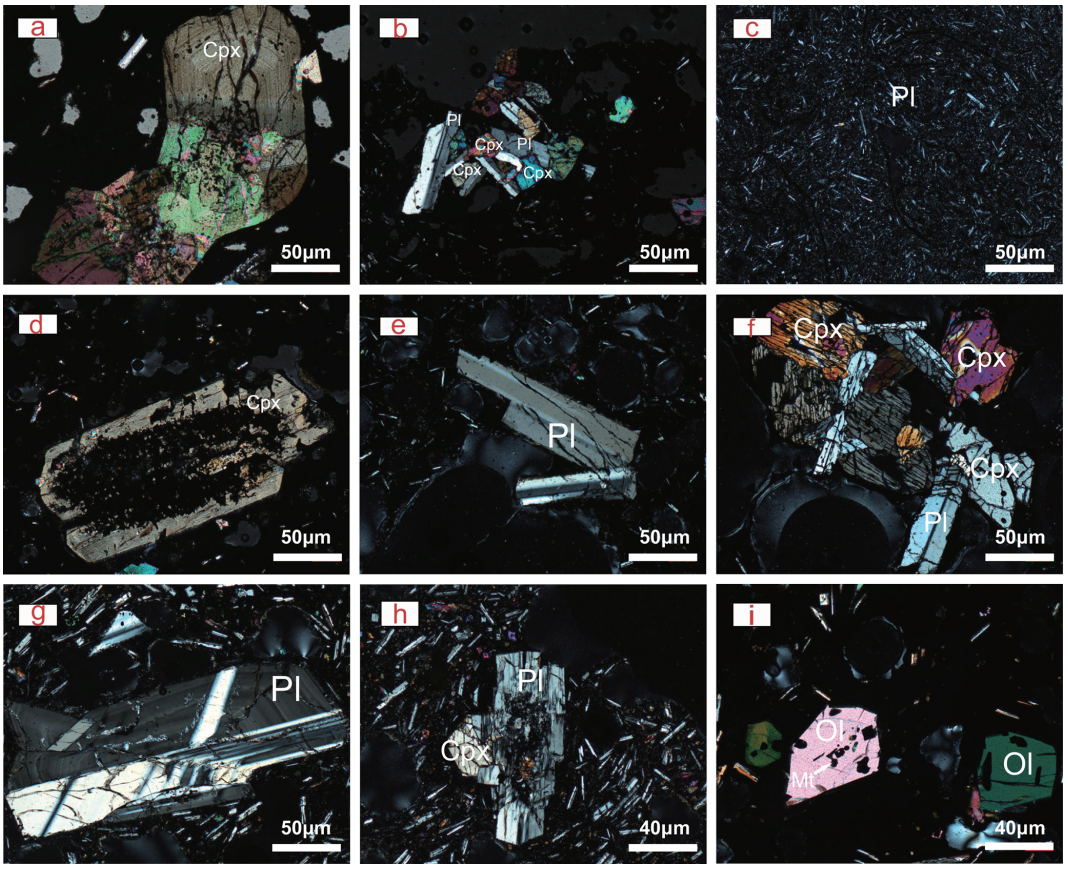

Figure 3. Representative photomicrographs of volcanic rocks in the WVF under cross-polarized light. **(a)** Zoned clinopyroxene-dominated glomerocryst from NLDL. **(b)** Glomerocryst of plagioclase and clinopyroxene from NLDL. **(c)** Plagioclase-dominated matrix from NLDL. **(d)** Large sieve-textured clinopyroxene phenocryst from ZLDL. **(e)** Euhedral, homogeneous plagioclase phenocryst from HNB. **(f)** Glomerocrysts containing clinopyroxene and plagioclase, from HNB. **(g)** Oscillatory zoned plagioclase phenocryst from HSS. **(h)** Subhedral plagioclase phenocryst with strongly sieve-textured core from HSS. **(i)** Euhedral olivine phenocrysts with oxide mineral inclusions from HS. Abbreviations: Ol, olivine; Cpx, clinopyroxene; Pl, plagioclase; Mt, magnetite.

Table 2. Summary of the mineral assemblage of the WVF.

Volcano	Clinopyroxene				Plagioclase			
	Type 1	Type 2	Type 3	Type 4	Type 1	Type 2	Type 3	Type 4
Beiliandanlu	×	×					×	
Zhongliandanlu	×	×	×	×	×	×	×	×
Nanliandanlu	×	×	×	×	×	×	×	×
Huoshaoshan	×	×	×		×	×	×	×
Heinaobao	×	×	×		×	×	×	
Hongshan	×	×	×		×		×	

4.1.3 Plagioclase composition

Plagioclase is the most abundant mineral and appears as euhedral to sub-euhedral phenocrysts, glomerocrysts and groundmass. The compositions of plagioclase are listed in Table S4. Phenocrysts show a range of compositions from An_{44} to An_{63} (An is molar Ca/(Ca + Na); Fig. 4e). The majority of plagioclase from the WVF tightly converges at $An_{55–60}$, belonging to labradorite, except a small amount of NLDL plagioclase is in the range of $An_{44–47}$ as andesine (Fig. 4b and e).

Comparable with the clinopyroxene, plagioclase typically displays complex zoning patterns, including normal, reverse and oscillatory zoning as well as sieve and resorption/em-

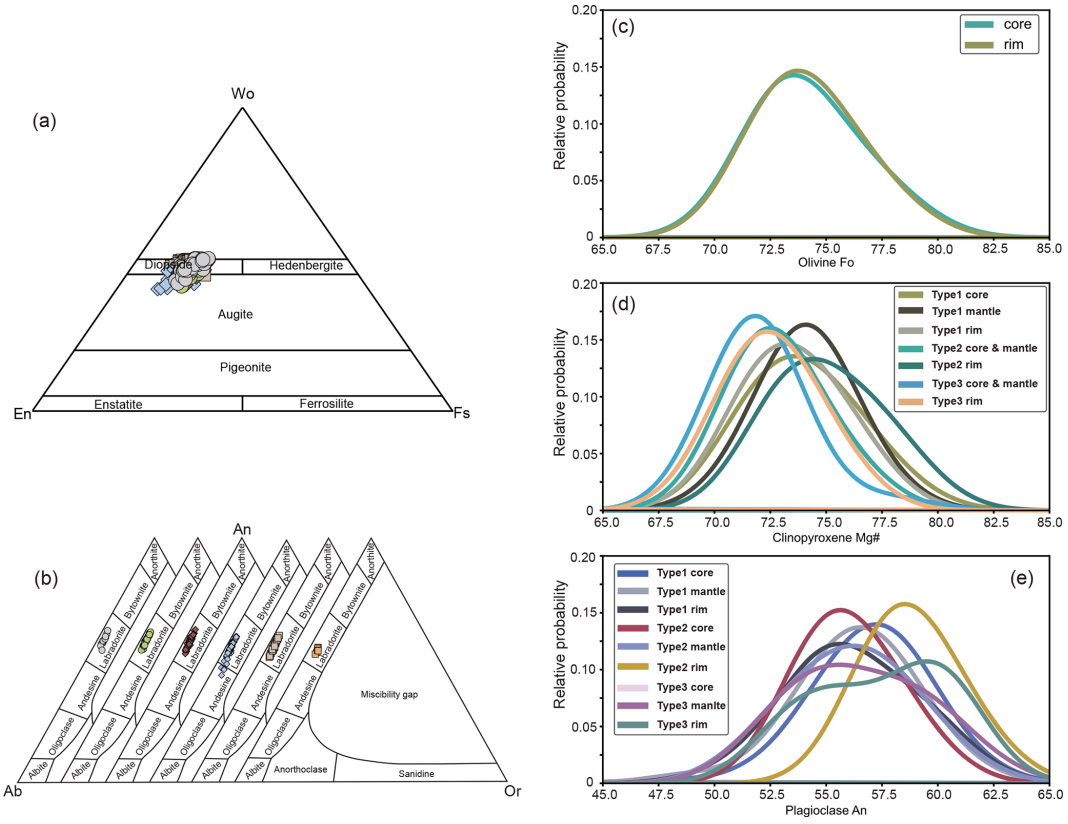

Figure 4. Major element composition of main mineral phases observed in the WVF. **(a)** Compositional classification diagram of pyroxene. **(b)** An–Ab–Or ternary classification diagrams of feldspar. Kernel density estimation (KDEs) for Fo content of olivine **(c)**; Mg# values of clinopyroxene **(d)**; An content of plagioclase **(e)**.

bayed textures. Plagioclase crystals in glomerocrysts are also predominantly homogeneous and/or slightly zoned, in some cases, representing the dominant mineral phase within the glomerocryst (Fig. 3b). Based upon textural investigation and core-to-rim compositional profiles of plagioclase crystals, the plagioclase phenocrysts are divided into four groups which are consistent with those of the clinopyroxene.

1. Type 1 plagioclase (Pl-1) is the ubiquitous phase in the plagioclase population, which is characterized by absence of zonation or normally zoned with slightly decreasing An content ranging from 58 to 54 along the core-to-rim profile (Fig. 5b). An content of Type 1 ranges from 47–63 with a peak of 57.

2. Type 2 plagioclase (Pl-2) constitutes 10 % of the studied plagioclase of the samples in the WVF. An content of Type 2 ranges from 51–62 with a peak of 56. It is characterized by a low An_{53} core surrounded by a more calcic rim, i.e., An_{58}. Notably, the crystals with reversal zonation have euhedral shape rims and exhibit gradually compositional variations (Fig. 5d).

3. Type 3 plagioclase (Pl-3) with oscillatory zoning is characterized by faint oscillations and extensive oscillations of the An content in the compositional interval $An_{53–60}$. Core-to-rim composition profiles have even shown the occurrence of two different extents of oscillation of the An content, ranging from $\sim \Delta An_{2–4}$ and $\sim \Delta An_{3–7}$ (Δ represents variation in An content; Fig. 5f). An content of Type 3 ranges from 52–62 with a peak of 57.

4. Type 4 plagioclase (Pl-4) with resorbed/embayed crystals is characterized by the resorption of all the crystals or of most of their cores and is encircled by a narrow euhedral rim (Fig. 3h), accounting for ~ 5 % of the plagioclase population.

4.1.4 Fe–Ti oxides

Fe–Ti oxides occur as subhedral phenocryst and groundmass distributed in the groundmass and as inclusions in the phenocryst mineral like olivine or clinopyroxene. No exsolution lamellas were observed among the oxides.

4.2 Bulk rock major and trace element characteristics

Bulk rock major and trace element concentrations are reported in Table S1. The studied samples fall into the tra-

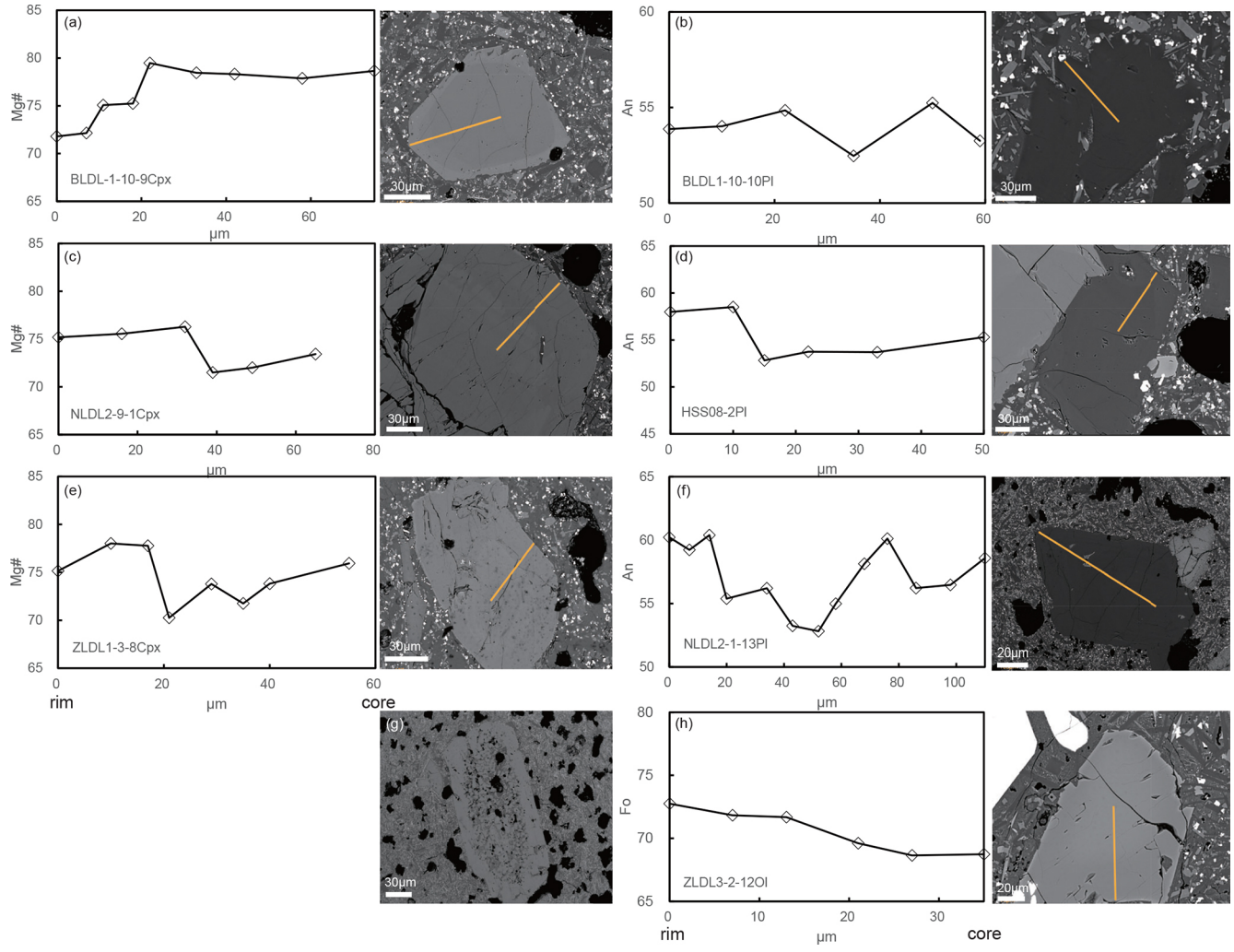

Figure 5. Rim-to-core compositional profiles of representative olivine, clinopyroxene and plagioclase crystals from the WVF. Yellow lines in BSE images mark measured line profiles. **(a)** A representative normal-zoning trend of clinopyroxene from BLDL, with a high Mg# core surrounded by a narrow low-Mg#-overgrowth rim. **(b)** Normally zoned An mole percent profiles of plagioclase from BLDL. **(c–d)** Example of reverse-zoned clinopyroxene and plagioclase from NLDL and HSS, respectively, characterized by Mg-poor or An-poor cores surrounded by Mg-rich or An-rich rims. **(e–f)** Complexly zoned clinopyroxene and plagioclase, showing a normal composition core or Mg-rich cores with the mantle displaying variable reverse or normal zoning in ZLDL and NLDL, respectively. **(g)** Sieve-textured clinopyroxene from ZLDL. **(h)** Reverse-zoning olivine from ZLDL, with Mg# continuously rising from core to rim.

chybasalt, basaltic trachyandesite, and boundary between phonotephrite and tephrite fields on the silica-vs.-total alkali classification diagram (TAS diagram; Le Bas et al., 1986; Fig. 6a). Moreover, on the K_2O-vs.-SiO_2 diagram (Peccerillo and Taylor, 1976; Fig. 6b), the compositions of BLDL, ZLDL, HNB, HS and HSS samples lie on the shoshonitic series, except for NLDL samples that, being lower in K_2O, are plotted into the high-K calc-alkaline series. Furthermore, the BLDL, ZLDL, HNB, HS and HSS samples are characterized by relatively low SiO_2 (46.9 wt %–49.9 wt %), MgO (3.9 wt %–4.6 wt %), CaO (7.6 wt %–8.7 wt %), Mg# (41.1–46.0; Mg# is molar $100 \times Mg/(Mg + Fe)$) and Sc (11–18 ppm), with high alkalinity and TiO_2 (2.3 wt %–2.7 wt %) and P_2O_5 (0.7 wt %–1.0 wt %). In contrast, the NLDL samples have low alkalinity with relatively high Mg# (45.9–50.0) and relatively high SiO_2 (48.5 wt %–50.3 wt %), MgO (4.9 wt %–6.0 wt %), CaO (8.1 wt %–8.4 wt %) and Sc (12–19 ppm) and low TiO_2 (2.2 wt %–2.3 wt %) and P_2O_5 (0.56 wt %–0.6 wt %). In addition, the primitive-mantle-normalized values of trace element abundances show enrichment of large-ion lithophile elements (LILEs) such as Rb, Ba, Sr and K. In chondrite-normalized rare earth elements (REEs), patterns are enriched in light rare earth elements (LREEs) relative to heavy rare earth elements (HREEs; Fig. 7a and b) with $(La/Yb)_N$ of 18.3–29.5 (N means chondrite-normalized values). Our new analyses are

consistent with the previous reported data of the WVF (e.g., Fan et al., 2014; Zhao et al., 2019).

5 Discussion

5.1 Thermobarometry calculations for pre-eruptive *P–T* conditions

5.1.1 Clinopyroxene–melt thermobarometry

In this study, we use the pressure-sensitive thermometer of Putirka (2008, Eq. 33) with the temperature-sensitive barometer of Neave and Putirka (2017) based on the jadeite and diopside–hedenbergite exchange equilibria between clinopyroxene and coexisting melt iteratively to determine the *P–T* crystallization condition of clinopyroxene which crystallized from the WVF magmas. These formulations produce a standard error of estimate (SEE) of ±1.4 kbar and ±45 °C, respectively. In order to refine our thermobarometry estimates, all clinopyroxene–melt pairs were assessed for chemical equilibrium before calculating *P–T* conditions by applying the following criteria: (1) the observed Di–Hd components of clinopyroxene are within 10 % of the values predicted by the model of Putirka (1999; Fig. 8a) and (2) the equilibrium constant for Fe–Mg exchange $Kd^{Fe\text{-}Mg}_{cpx\text{-}liq}$ is in the range of 0.27 ± 0.03 (Neave and Putirka, 2017; Fig. 8b). All results derived under these parameters/conditions which yielded negative pressure values and/or are out of the predicted equilibrium range (ΔDiHd > 10 %) are considered unreliable here and will be discarded in the further discussion.

The clinopyroxene–melt thermobarometric estimation results are displayed in Table 3, and the relative probability density curves of the thermobarometry data are highlighted by kernel density estimate (KDE) plots (Fig. 9). The temperature estimates derived from the Type 1, 2 and 3 clinopyroxene–melt pairs show a distribution peak value of 1115–1130 °C (Fig. 9). The pressure estimates derived from the Type 1, 2 and 3 clinopyroxene–melt pairs show a distribution peak value of 9–10 kbar except Type 1 and Type 2 of NLDL with a peak value of 6.0–6.7 kbar. Considering the SEE of ±45 °C and ±1.4 kbar for the clinopyroxene–melt thermobarometry (Neave and Putirka, 2017), this means that all samples have a similar clinopyroxene crystallization temperature in the range of 1115–1130 °C. Besides, the BLDL, ZLDL, HSS, HNB and HS show similar clinopyroxene crystallization pressure with a range of 9–10 kbar except NLDL, which has a lower pressure cluster at ∼ 6.0–6.7 kbar.

5.1.2 Plagioclase–melt thermometry

Further constraints on magma storage conditions and differentiation processes can be obtained through the combination of other mineral–melt thermobarometers. We apply Eq. (24a) (SEE of ±36 °C) of the plagioclase–melt equilibrium thermometer of Putirka (2008) based on temperature-sensitive volumetric and compositional changes associated with anorthite (An)–albite (Ab) exchange.

Plagioclase and bulk rock composition yield anorthite (An)–albite (Ab) partitioning coefficient $Kd^{An\text{-}Ab}_{plag\text{-}liq}$ values ranging from 0.19 to 0.43, well consistent with the equilibrium value of 0.27 ± 0.11 suggested for temperatures > 1050 °C (Putirka, 2008). Hence, the plagioclase that does not fall into the equilibrium field will be not considered in this study. Furthermore, the KDE plots of plagioclase–melt thermometer data are shown in Fig. 10, and the calculation results are present in Table 3. The temperature estimations derived from the Type 1, 2 and 3 plagioclase–melt pairs show a distribution peak value of 1126–1132 °C except those of NLDL with a peak value of 1100–1105 °C. Considering the error of the plagioclase–melt thermometer, the plagioclase crystallization temperatures are estimated to be in the range of 1100–1132 °C.

5.1.3 Olivine–melt thermometry

The olivine–melt equilibrium thermometer, i.e., Eq. (22) of Putirka (2008) with SEE of ±43 °C, was applied in this study to obtain the crystallization temperature of olivine in our samples. Olivine–melt equilibrium is based on the relatively invariant exchange coefficient $Kd^{Fe\text{-}Mg}_{ol\text{-}liq} = 0.30 \pm 0.03$, used to constrain the crystallization temperature range (Fig. 8c; Putirka, 2008; Roeder and Emslie, 1970). Considering the relatively small fraction of phenocryst contents and lack of quenched glass or melt inclusion, we used bulk rock composition as the melt component, assuming 2 wt % H_2O in melt based on the result of clinopyroxene hygrometry (Perinelli et al., 2016) and plagioclase hygrometry (Putirka, 2008) for these thermobarometry model calculations as discussed below. Particularly, most of the olivine compositions are in the equilibrium range and values over the Kd criteria are discarded (Fig. 8c). The kernel density estimates (KDEs) of olivine equilibrium temperature derived from the olivine core and rim of BLDL, ZLDL, HSS, HNB and HS show a distribution peak value of 1134 °C except NLDL with a peak value of 1160 °C. The difference generally lies in analytical uncertainty (±43 °C), indicating that the WVF has a similar olivine crystallization temperature in the range of 1134–1160 °C.

5.1.4 Melt water content

Melt water contents of our samples from the WVF were estimated by the plagioclase–melt hygrometer of Putirka (2008, Eq. 25b) which was calibrated based on anorthite–albite exchange reaction between crystal and melt with a relatively high SEE of ±1.1 wt %, as well as the clinopyroxene–melt hygrometer of Perinelli et al. (2016) with an SEE of ±0.5 wt %.

The results are listed in Table 3, and KDE plots are displayed in Figs. 9 and 10. The results show that all types

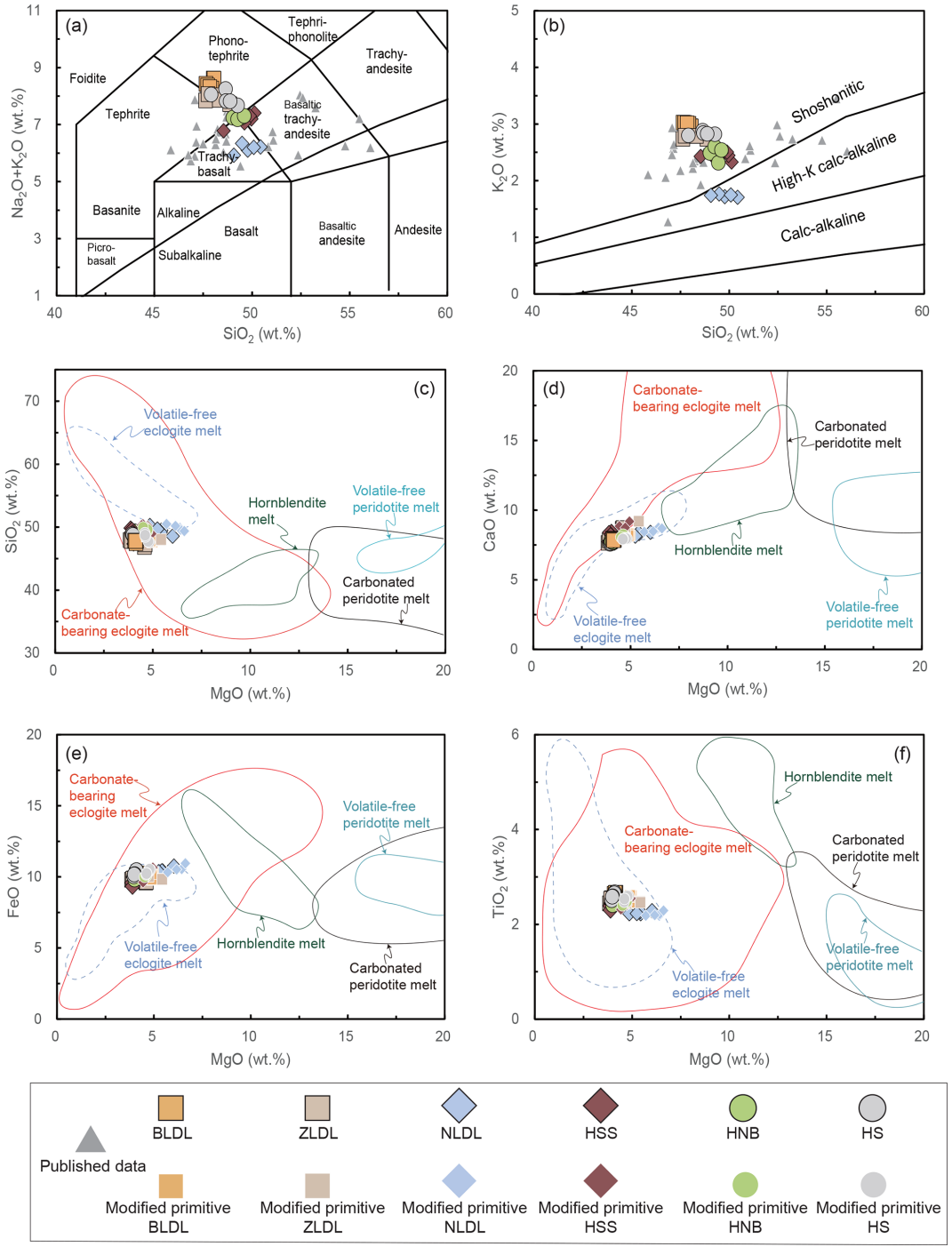

Figure 6. **(a)** Total alkali–silica (TAS) diagram (after Le Bas et al., 1986, and the line divides alkaline and sub-alkaline rocks after Irvine and Baragar, 1971) for volcanic rocks in the WVF. **(b)** K_2O-vs.-SiO_2 correlation diagram (after Peccerillo and Taylor, 1976). **(c)** SiO_2 vs. MgO. **(d)** CaO vs. MgO. **(e)** TFeO vs. MgO. **(f)** TiO_2 vs. MgO. Published literature data of the WVF are compiled from Fan et al. (2014) and Zhao et al. (2019). Also shown for comparison are experimental silicate melts and carbonated silicate melts of carbonate-bearing eclogites (Dasgupta et al., 2006; Gerbode and Dasgupta, 2010; Litasov et al., 2011; Kiseeva et al., 2012; Thomson et al., 2016; Elazar et al., 2019) and carbonate-bearing peridotites (Hirose, 1997; Dasgupta et al., 2007; Foley et al., 2009; Litasov et al., 2011; Dasgupta et al., 2013; Ghosh et al., 2014; Dvir and Kessel, 2017; Pinté et al., 2021), hornblendite (Pilet et al., 2008), volatile-free eclogites (Yaxley and Green, 1998; Pertermann and Hirschmann, 2003; Spandler et al., 2008), and volatile-free peridotites (Takahashi and Kushiro, 1983; Takahashi and Scarfe, 1985; Hirose and Kushiro, 1993; Takahashi et al., 1993; Walter, 1998; Davis et al., 2011) at > 2.5 GPa. The symbols with a black line represent the whole rock composition of the WVF, and the symbols with a white line represent the primitive melt composition after fractional crystallization correction (see details below).

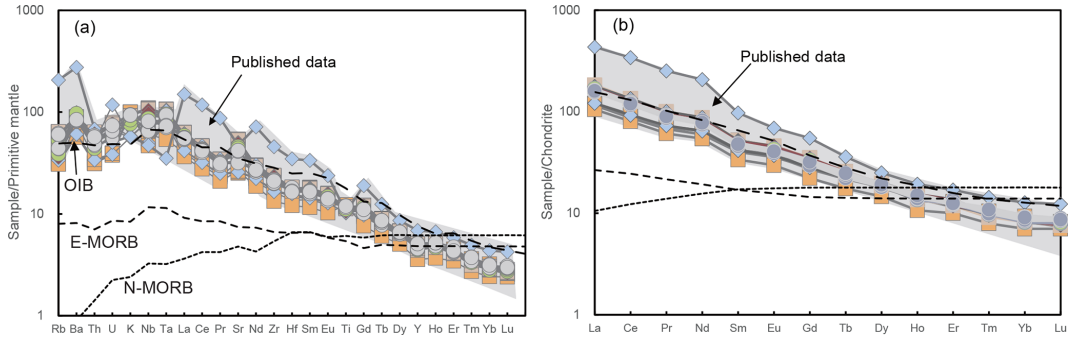

Figure 7. **(a)** Primitive-mantle-normalized multi-element diagrams (normalization values are after Sun and McDonough, 1989). **(b)** Chondrite-normalized REE patterns of the WVF volcanic rocks (normalization values are after Sun and McDonough, 1989). The values of OIB (ocean island basalt), N-MORB (normalized mid-ocean ridge basalt) and E-MORB (enriched mid-ocean ridge basalt) from Sun and McDonough (1989) are shown by the dashed lines. Symbols and fields are the same as in Fig. 6.

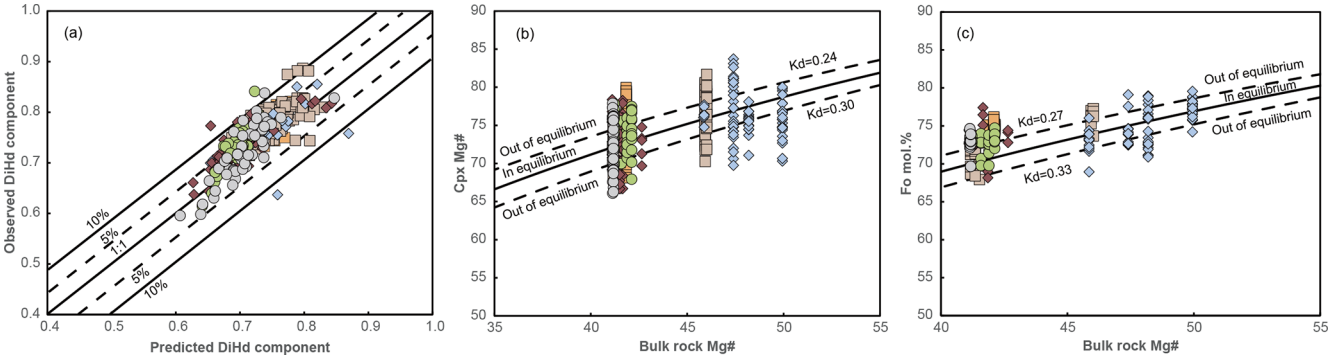

Figure 8. Tests for equilibrium between clinopyroxene or olivine and nominal melts. **(a)** Predicted vs. observed clinopyroxene mineral components (diopside–hedenbergite). The equilibrium region requires $\Delta\text{DiHd} \leq 0.1$. **(b)** Rhodes diagram for clinopyroxene from the WVF showing equilibrium $\text{Kd}^{\text{Fe-Mg}}_{\text{cpx-liq}}$ curve of 0.27 (solid line) and error limits of ± 0.03 (dashed lines) after Neave and Putirka (2017). **(c)** Rhodes diagram for olivine from the WVF; the continuous curves represent the equilibrium $\text{Kd}^{\text{Fe-Mg}}_{\text{ol-liq}}$ of 0.3, while the dashed lines represent the error intervals of ± 0.03 (Putirka, 2008).

of minerals have a similar H_2O content. Specifically, the plagioclase–melt hygrometer results of Type 1, 2 and 3 cluster at 1.1 wt %, which is systematically lower than those of the clinopyroxene–melt hygrometer of Type 1, 2 and 3 by ~ 1.2 weight percentage points. The reason for this deviation may be attributed to the inherent errors of the hygrometer. Therefore, we consider that the 1.1 wt %–2.3 wt % H_2O content in the melt is reasonable.

5.2 Magma plumbing system of the WVF

Based on the above thermobarometers and melt water content estimation, it is postulated that there are two distinct magma storage zones at depths with similar temperature and water content, with a deeper region at the lower crustal levels or near the crust–mantle boundary ($\sim$ 33–36 km; the convert equation of pressure to depth and the densities of the representative crustal and mantle layers beneath eastern China are from Sun et al., 2018) for BLDL, ZLDL, HSS, HNB and HS volcanoes and a second reservoir at mid-crustal levels ($\sim$ 23–26 km) for the NLDL volcano. Four types of clinopyroxene and plagioclase phenocrysts in the WVF not only record the information about crystallization conditions but also yield a wealth of information about the processes within the magma plumbing system as reflected by their compositional growth zonation (e.g., Kahl et al., 2011; Ubide et al., 2014; Howarth and Taylor, 2016; Crossingham et al., 2018).

Particularly, in this study, the Type 1 of clinopyroxene and plagioclase is characterized by normal zoning as shown in Fig. 5a–b, suggesting that they crystallized in magma reservoirs involving fractional crystallization processes. In contrast, the Type 2 of clinopyroxene and plagioclase comprises typical reverse-zoned crystals (Fig. 5c–d) where relatively Mg- and An-rich rims are observed. Combined with the presence of some reverse-zoned olivine phenocrysts, it is reasonable to believe that primitive magma recharge and mixing occurred during the evolution of the magmatic plumbing system for the WVF (e.g., Streck, 2008; Longpré et al., 2014; Neill et al., 2015; Gernon et al., 2016; Ubide and Kam-

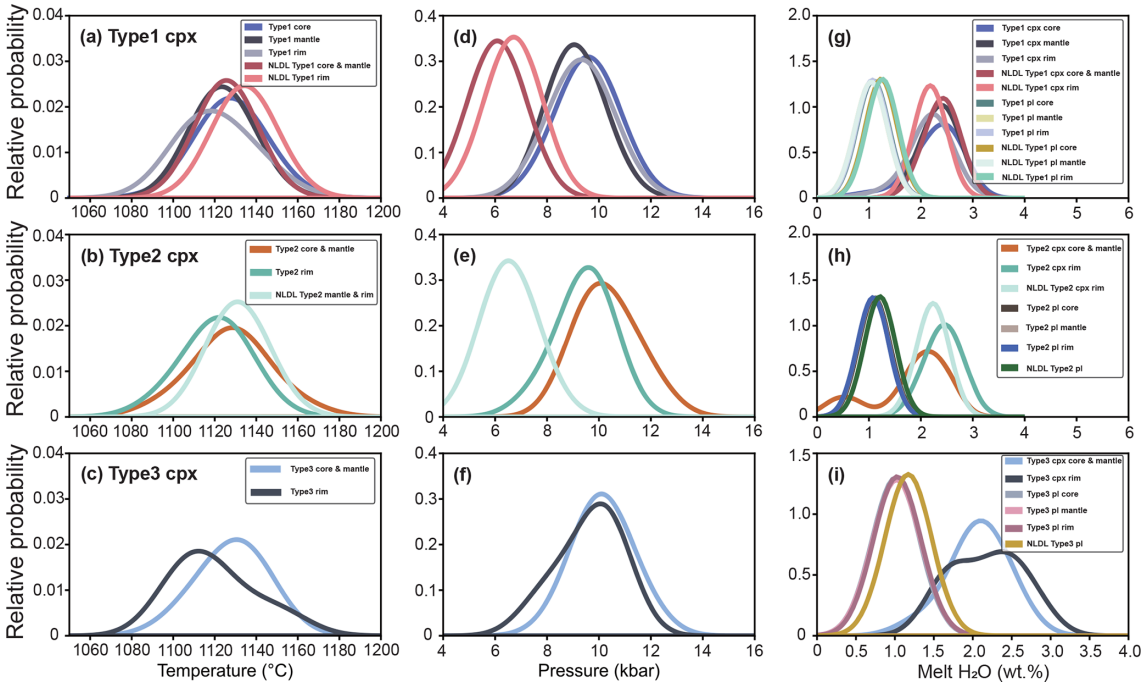

Figure 9. Kernel density estimates (KDEs) of thermobarometric and hygrometric calculation results for the Type 1 **(a, d, g)**, Type 2 **(b, e, h)** and Type 3 **(c, f, i)** of clinopyroxene and plagioclase **(g, h, i)** in the WVF. Crystallization temperatures and pressures are calculated following the clinopyroxene–melt thermobarometer of Neave and Putirka (2017). The melt water contents are following the clinopyroxene–melt hygrometer of Perinelli et al. (2016) and plagioclase–melt hygrometer of Putirka (2008).

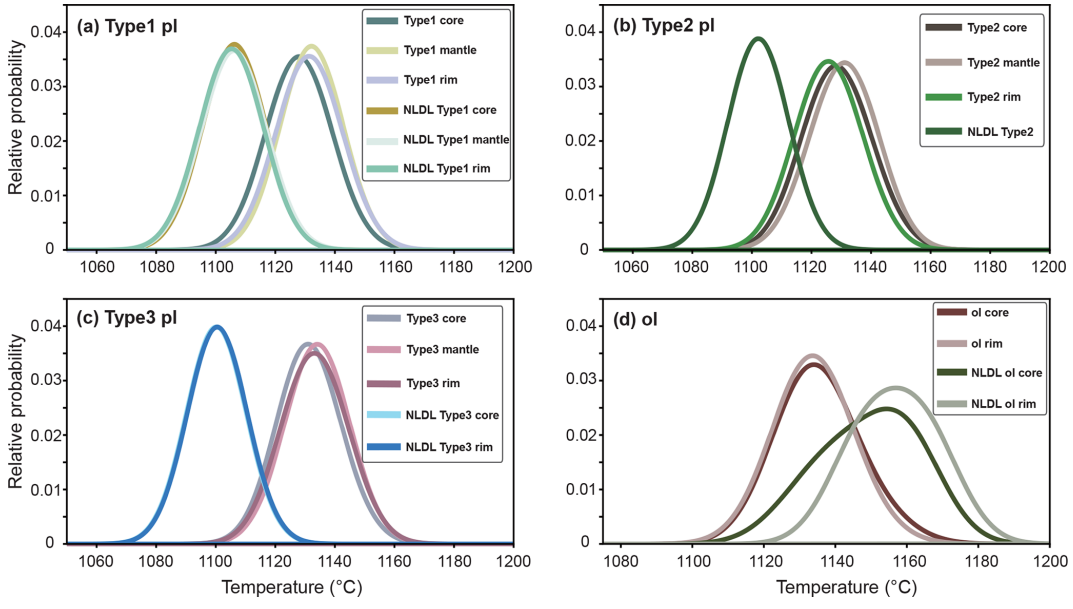

Figure 10. Kernel density estimates (KDEs) of thermometric calculation results for plagioclase **(a–c)** and olivine **(d)** in the WVF. Crystallization temperatures are calculated following the plagioclase–melt thermometer of Putirka (2008) and olivine–melt thermometer of Putirka (2008).

Table 3. Geothermobarometry and hygrometry estimations derived for samples from the WVF based on various olivine, clinopyroxene and plagioclase models.

	Olivine–melt (Putirka, 2008)		Clinopyroxene–melt (Neave and Putirka, 2017)		P (kbar)	P_{Peak}	Clinopyroxene–melt (Perinelli et al., 2016)		Plagioclase–melt (Putirka, 2008)		H_2O (wt %)	H_2O_{Peak}
	T (°C)	T_{Peak}	T (°C)	T_{Peak}			H_2O (wt %)	H_2O_{Peak}	T (°C)	T_{Peak}		
SEE	±43 °C		±45 °C		±1.4		±0.5		±36 °C		±1.1	
Type 1	1120–1156	1134	1090–1157	1123	7.3–11.6	9.4	0.6–4.9	2.3	1118–1143	1129	0.9–1.2	1.1
Type 2			1097–1159	1125	7.7–12.1	9.8	0.3–2.8	2.3	1117–1141	1126	0.9–1.2	1.1
Type 3			1104–1150	1134	7.9–11.8	10.0	1.3–2.7	2.1	1126–1141	1132	0.9–1.1	1.0
NLDL	1125–1165	1160	1110–1144	1128	4.8–7.7	6.2	1.9–3.3	2.2	1099–1111	1105	1.1–1.5	1.2

ber, 2018). In addition, oscillatory compositional zonation is also observed in the Type 3 of clinopyroxene and plagioclase (Fig. 5e–f), which could be interpreted either by small-scale crystallization kinetic effects at the crystal–melt interface or by repeated changes in the physicochemical conditions controlled by external parameters (e.g., Shore and Fowler, 1996; Ginibre et al., 2002). Nevertheless, the small-scale crystallization kinetics model is more suitable for the small-scale and low-amplitude fine banding rather than relatively large zonation width and composition variation (Elardo and Shearer, 2014). Therefore, repeated and periodic magma replenishment and magma convection could account for the oscillatory bands with relatively large Mg# or An variation ($\Delta > 8$) in the Type 3 of clinopyroxene and plagioclase. Such an inference involving primitive magma recharge is further supported by the sieve texture observed in the Type 4 of clinopyroxene and plagioclase (Figs. 3h and 5g).

5.3 Identification of carbonate-bearing eclogite mantle source

Based on the bulk rock trace elements and the Sr–Nd–Pb–Hf–Mg isotopic compositions, previous studies have suggested that the Wulanhada alkaline basalts with low MgO contents formed by fractional crystallization of primary melt produced by relatively low degree partial melting of carbonated peridotite (e.g., Fan et al., 2014; Zhao et al., 2019; Sun et al., 2021). To further constrain the mantle source of the WVF, we evaluated the inverse fractional crystallization processes by adding proportions of olivine, clinopyroxene and plagioclase as observed in our samples (Table 1; see Armienti et al., 2013, for the details of calculations), obtaining the primary melt compositions in equilibrium with the most primitive clinopyroxene and olivine (Fig. 6; Table S5). The Wulanhada primitive melt composition shows low MgO (4.4 wt %–6.6 wt %), Mg# (44–52) and CaO/Al_2O_3 (0.5–0.6) and relatively high TiO_2 (2.2 wt %–2.6 wt %) content (Table S5), which is similar to the Cenozoic intraplate Hannuoba alkaline basalts in eastern China (Fig. 1; 25–14 Ma; Liu et al., 1992; Zhou and Armstrong, 1982) derived from partial melting of carbonated eclogite (Zou et al., 2022). Additionally, the primitive melt compositions are also consistent with those experimentally produced for carbonate-bearing eclogite partial melts (Fig. 6).

For comprehensive evaluations of the mantle source lithology in the WVF, we use various discrimination parameters as follows. Pyroxene has high Ca but low Fe/Mn and Zn/Fe partition coefficients; the melts derived from pyroxenite will show low CaO contents but high Fe/Mn and Zn/Fe ratios (Hirschmann et al., 2003; Kogiso et al., 2003; Sobolev et al., 2005; Herzberg, 2006; Sobolev et al., 2007); the Wulanhada basalts are mainly located in the pyroxenite-derived melt field (Fig. 11a and b). The FCKANTMS parameter is proposed by Yang et al. (2019) based on the experimental melt composition derived from a variety of mafic and ultramafic lithologies, is not sensitive to temperature and pressure, and can distinguish effectively peridotite-derived melt from pyroxenite- and hornblendite-derived melt. The Wulanhada basalts are in the field of non-peridotite (Fig. 11d), indicating the presence of mafic lithology in the source. Alternatively, the Wulanhada basalts are consistent with experimental carbonate-bearing eclogite-derived melts in the CIPW normative composition diagram (Fig. 11c). Based on these discrimination parameter diagrams, it appears that carbonate-bearing eclogite may exist in the mantle source of the WVF, which is further supported by Wulanhada basalts with a lower bulk rock Mg isotopic composition ($\delta^{26}Mg = -0.51‰$ to $-0.32‰$; Sun et al., 2021) than depleted mantle ($\delta^{26}Mg = -0.25 \pm 0.04‰$; Teng et al., 2010).

5.4 Source lithology and mantle processes

In order to further constrain the mantle source characteristics of Wulanhada alkaline basalts, a non-modal batch melting model is employed to simulate the partial melting of carbonate-bearing eclogite (Fig. 12; Shaw, 1970; see Zou et al., 2022, for the details of the calculations). A quantitative calculation of the mineral assemblages of carbonate-bearing eclogite can be achieved by using diagnostic ratios such as Zr/Hf (clinopyroxene-sensitive; Pertermann et al., 2004),

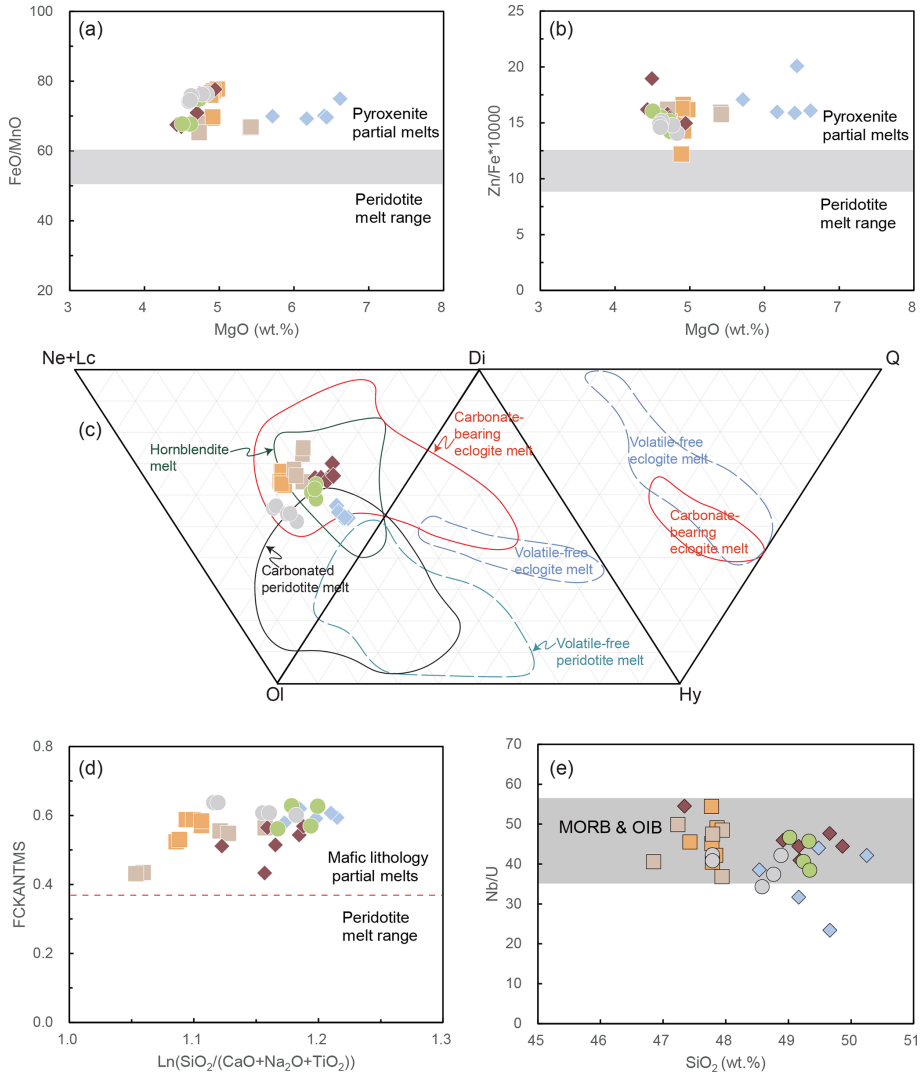

Figure 11. Geochemical compositional indicators of mantle source lithology and crustal contamination. **(a)** FeO/MnO and **(b)** Zn/Fe × 10 000 vs. MgO; the boundary field between the peridotite melt range and pyroxenite melt are after Herzberg (2011) and Le Roux et al. (2010), respectively. **(c)** CIPW normalization plotted on Ne + Lc (nepheline + leucitite), Ol (olivine), Di (diopside), Hy (hypersthene), Q (quartz) and the fields for experimental melting data as outlined in Fig. 6. **(d)** FCKANTMS parameter vs. $\mathrm{Ln(SiO_2/(CaO+Na_2O+TiO_2))}$; the FCKANTMS parameter calculation and discrimination line for mafic lithology-derived melts are from Yang et al. (2019). **(e)** Nb/U vs. $\mathrm{SiO_2}$; the shaded field for MORB (mid-ocean ridge basalt) and OIB is from Hofmann et al. (1986). Symbols and fields are the same as in Fig. 6.

Ti/Eu (carbonate-sensitive; Rudnick et al., 1993; Dasgupta et al., 2009) and Dy/Yb (garnet-sensitive; Klemme et al., 2002; Pertermann et al., 2004). The calculation results show that the Wulanhada alkaline basalts formed by a relatively high degree of partial melting (10 %–20 %) of carbonate-bearing eclogite (Fig. 12; ∼ 3 wt % carbonate; Gt/Cpx = 2 : 8, where Gt denotes garnet and Cpx denotes clinopyroxene), as the solidus of carbonate-bearing eclogite is lower than that of peridotite (Hirschmann et al., 2003; Thomson et al., 2016). Considering the chemical disequilibrium between primary low-MgO alkaline basalts and peridotite, the upward migration of primary melt may interact with the overlying lithospheric mantle (Lambart et al., 2013; Sakuyama et al., 2013; Zhang et al., 2017). For example, Cenozoic alkaline basalts from Datong and Hannuoba in eastern China are considered to interact with the lithospheric mantle during ascent from source to surface (Fig. 1; Xu et al., 2005; Wang and Liu, 2021; Zou et al., 2022). During the melt–peridotite interaction, peridotite components were introduced into the reactive melt and modified the MgO and alkali contents of melt (Kogiso et al., 2004; McGee et al., 2013; Pontesilli et al., 2021). Nanliandanlu samples exhibit higher MgO and lower alkali contents than the samples from the other five volcanoes (Fig. 6), which may be attributed to the interaction between

primary melt and the lithospheric mantle during ascent to the surface (Fig. 13). The interaction resulted in an increase in MgO and a decrease in the alkaline contents of Nanliandanlu magma, which is consistent with the mechanism that the lithospheric mantle acts as a filter for the composition and alkalinity of the Dunedin volcano in New Zealand (Pontesilli et al., 2021).

The Wulanhada region experienced the southward subduction of the Paleo-Asian plate beneath the North China Craton and collision to form the Central Asian Orogenic Belt from the late Paleozoic to the early Mesozoic (Yang et al., 2006; Zhang et al., 2009). It has also been affected by the westward subduction of the Paleo-Pacific plate since the Cretaceous (Niu, 2005; Wu et al., 2005). Based on the low bulk rock Mg isotopic composition of the Wulanhada basalts, Sun et al. (2021) speculated that these rocks may be related to the subduction of the ancient Pacific plate, through the eastward retreat of slab or detachment into the lower mantle. However, according to the carbonate xenoliths exposed in Cenozoic Hannuoba basalts in eastern China, Chen et al. (2016) suggested that the carbonates originated from subduction of the Paleo-Asian plate rather than the Paleo-Pacific plate. A precise date of the carbonate xenoliths exposed in the Wulanhada region is required to determine the subduction event. However, it is possible that the subducted slab carried a large volume of carbon into the mantle, which remained in the deep mantle as carbonated eclogite (Hammouda, 2003; Dasgupta et al., 2004). In addition, the fluids released from the subducted slab infiltrated the lithospheric mantle, resulting in the development of amphibolite and pyroxenite veins with signatures of subduction (Niu and O'Hara, 2003; Pilet et al., 2008; Shea and Foley, 2019; Brenna et al., 2021). The carbonate-bearing eclogite-derived melts assimilated the metasomatic veins during ascent to the surface, resulting in the subduction-related signature with Nb–Ta negative anomalies and Rb–Ba enrichment as displayed by the sample from Nanliandanlu (Fig. 7).

5.5 Trigger of intraplate monogenetic volcanism in the WVF

In addition to the uplift of the Tibetan Plateau and adjacent regions, the collision of the Indian and Eurasian plates also has an effect on volcanic activities thousands of kilometers away. For instance, Zhang et al. (2021) suggested that the far-field effect of the Indian–Eurasian collision plays an essential role in controlling the eruption of basalts in central Mongolia. Based on tectonic features, Zhao et al. (2019) suggested that the Wulanhada Volcanic Field was also influenced by the Indian–Eurasian collision. The asthenosphere flowed eastward due to the collision, causing the mantle potential temperature beneath the WVF to exceed the solidus of the mantle source lithology and promote partial melting (Liu et al., 2004). Due to the solidus of carbonated eclogite being lower than the anhydrous garnet peridotite (Hirose, 1997; Hammouda, 2003; Dasgupta et al., 2007), a relatively high degree (10 %–20 %) of partial melting occurred in the carbonate-bearing eclogite (~ 3 wt % carbonate; $\sim \mathrm{Gt/Cpx} = 2:8$) and the melt interacted with ambient peridotite. Melts ascended along the NE–SW-striking basement fault and the NW–SE-striking Wulanhada–Gaowusu fault under buoyancy force. The primitive magmas that formed the Hongshan, Huoshaoshan, Beiliandanlu, Zhongliandanlu and Heinaobao lavas ascended to the Moho (Fig. 13; 33–36 km depth), crystallizing olivine, clinopyroxene and plagioclase phenocrysts at the temperature ranges from 1100 to 1160 °C with melt water contents of 1.1 wt %–2.3 wt % (Figs. 9 and 10). The repeated magma replenishment resulted in the development of complex textures (Figs. 3 and 5; reverse and oscillatory zoning and sieve texture) and eventually triggered the eruption with increased magma temperature, buoyancy and overpressure. The deep faults acted as an ascending channel for magma, resulting in the distribution of volcanic cones parallel to the NE–SW and NW–SE striking.

The primitive magma of Nanliandanlu underwent more complex processes in comparison with those of the other five volcanoes. It interacted with the lithospheric mantle during ascent, which increased the MgO contents but decreased the alkaline contents in the melt. Additionally, the modified magma did not stagnate at the Moho but ascended along a secondary fault and was stored at the middle crust (Fig. 13; $\sim$ 23–26 km depth). Following the cooling of the magma, it crystallized olivine, clinopyroxene and plagioclase at the temperature range from 1100 to 1160 °C with melt water contents of 1.1 wt %–2.3 wt % (Figs. 9 and 10) and slightly assimilated crustal wall rocks, resulting in some samples with low Nb/U values (Fig. 11f). Repeated magma replenishment also took place in the Nanliandanlu magma reservoir to form the complex textures of the phenocrysts, and melt triggered the volcanic eruption. The crustal magma reservoir of the Nanliandanlu volcano in the WVF may represent a snapshot of the transition from monogenetic volcanoes to composite volcanoes. It is possible to form a composite volcano with large magma volumes and complex compositions if primary magmas are continuously supplied from the source and experience assimilation and fractional crystallization processes in the magma plumbing system.

5.6 The link between monogenetic and polygenetic volcanism

Elucidating the link between the monogenetic and the polygenetic volcanism has played an important role in understanding the evolution of magma and assessing the volcanic hazard (Brenna et al., 2010; Németh and Kereszturi, 2015; Cañón-Tapia, 2016; Smith and Németh, 2017). A sensu stricto monogenetic volcano is characterized by a single eruptive vent through which only a small and temporal magma supply of single composition or various compo-

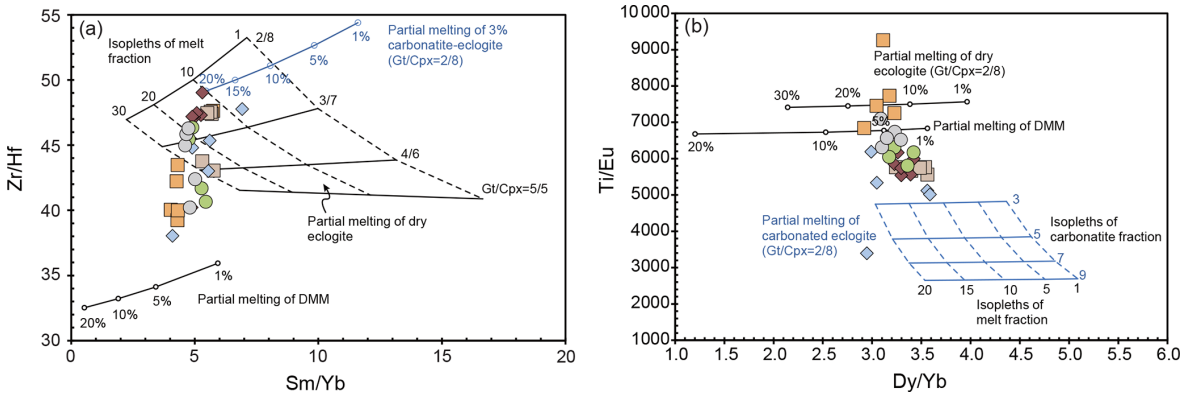

Figure 12. (a) Zr/Hf vs. Sm/Yb and **(b)** Ti/Eu vs. Dy/Yb in Wulanhada basalts, compared with calculated values using the non-modal batch melting model after Shaw (1970). For the details of calculation see Zou et al. (2022). Numbers against isopleths show the degrees of partial melting (black) and the amount of carbonatite in the source (blue). Data sources: carbonates (Hoernle et al., 2002), depleted MORB mantle (DMM; Workman and Hart, 2005) and MORBs (Gale et al., 2013).

sitions erupts once in a brief period of time (Németh and Kereszturi, 2015; Tchamabe et al., 2016). However, studies on monogenetic volcanoes of Rangitoto Island in the Auckland Volcanic Field, New Zealand, and Udo off Jeju Island, South Korea, have shown that the magma underwent fractional crystallization and magma mixing during ascent to the surface, which generated complex magma composition (Brenna et al., 2010; McGee et al., 2011). The Rangitoto and Udo monogenetic volcanoes represent a transition towards polygenetic volcanic systems. Primitive basaltic magma that underwent fractional crystallization, magma mixing and crustal contamination in the crustal magma reservoirs could generate polygenetic volcanoes with high magma supply and evolved composition (Smith and Németh, 2017), such as the polygenetic Ruapehu volcano in the Auckland Volcanic Field, New Zealand (Gamble et al., 2003; Lindsay et al., 2011).

A change in the local or regional stress field leads to the transition from polygenetic to monogenetic volcanism occurring in the Higashi-Izu region of Japan (Hasebe et al., 2001) and back-arc volcanism in southeast Guatemala (Walker et al., 2011). The increase in the crustal extension rate promotes the development of monogenetic volcanism (Takada, 1994; Bucchi et al., 2015). The tectonic setting and the local stress field control the genesis of some volcanic fields, such as in the San Francisco Volcanic Field (Arizona) where volcanism is thought to migrate with the westward movement of the North American Plate (Tanaka et al., 1986). The WVF could be the result of a far-field effect of the Indian–Eurasian collision (Zhao et al., 2019). On a local scale, the distribution of volcanic cones within a field can reveal the orientation of faults (Muffler et al., 2011). There are volcanic fields in which vents show a marked alignment normally associated with faults such as the Chaîne des Puys in France (Boivin and Thouret, 2014). The volcanic cones in the WVF are linearly distributed along the NE–SW-striking basement faults and the NW–SE-striking Wulanhada–Gaowusu fault (W–G fault) system. The structure of crust also has an effect on the genesis and evolution of the volcanic field (Smith and Németh, 2017). Magma moves upward driven by buoyancy and becomes stagnant at the density variation boundary, such as near the Moho and Conrad discontinuity, to form magma reservoirs (Sparks et al., 2018). Interestingly, the magma reservoirs in the WVF are located near the Moho and Conrad discontinuity, indicating that the structure of crust played an important role in the evolution of the WVF.

In summary, the WVF represents an example of the early stages of the transition from monogenic volcanoes to composite volcanoes. A change in regional tectonic stress resulted in partial melting of the mantle source and supplied the multi-level crustal magma reservoirs, where fractional crystallization, magma mixing and crustal contamination occurred. In this scenario, large volumes of magma in shallow zones of magma storage may evolve for long periods, eventually producing a polygenetic volcano with evolved magmas and large magma fluxes.

6 Conclusions

1. The primitive melts of Wulanhada alkaline basalts were produced by a relatively high degree (10 %–20 %) of partial melting of a carbonate-bearing eclogite (∼ 3 wt % carbonate; Gt/Cpx = 2 : 8).

2. The primitive magmas that formed the Hongshan, Huoshaoshan, Beiliandanlu, Zhongliandanlu and Heinaobao lavas ascended to the Moho (∼ 33–36 km depth) and crystallized olivine, clinopyroxene and plagioclase phenocrysts. However, the primitive magma of Nanliandanlu interacted with the lithospheric mantle during ascent, which increased the MgO contents but decreased the alkalinity of the melt. The modified

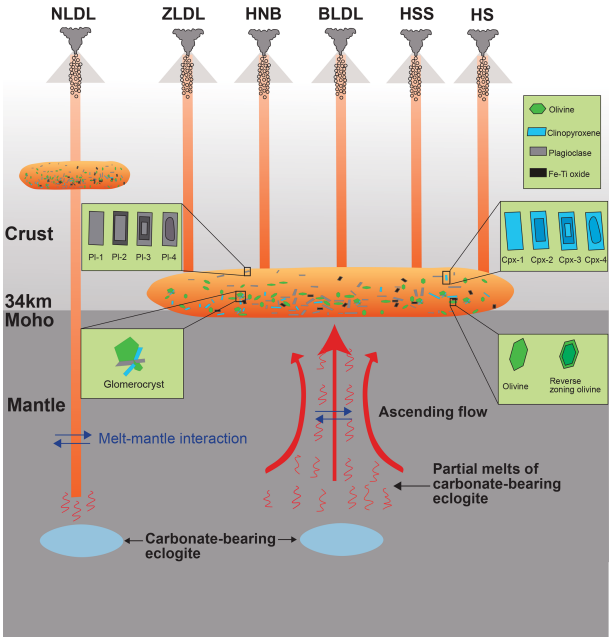

Figure 13. Schematic diagram of the magma plumbing systems beneath the Wulanhada Volcanic Field. Melt with a slightly higher degree of partial melting (∼ 10 %–20 %) of carbonate-bearing eclogite (∼ 3 wt %; Gt/Cpx = 2/8) is mixing with the relatively low degree of partial melting (∼ 5 %) of garnet peridotite. Mixing melt ascends to the Moho depth that crystallizes olivine, clinopyroxene, plagioclase and Fe–Ti oxide with conditions of ∼ 9–10 kbar (33–36 km) and ∼ 1100–1160 °C. The magmatic reservoirs in the Moho depth supply magmas for Beiliandanlu, Zhongliandanlu, Heinaobao, Huoshaoshan and Hongshan. With a difference, the primary melt of Nanliandanlu interacts with the mantle, which changes the melt composition during ascent from source to surface. Modified melt ascends to the middle crust depth that crystallizes olivine, clinopyroxene, plagioclase and Fe–Ti oxide with conditions of ∼ 6.0–6.7 kbar (23–26 km) and ∼ 1100–1160 °C. The relatively shallow magmatic reservoir supplies melt for Nanliandanlu. The injection of melt from the mantle source into the two magmatic reservoirs results in the complex mineral textures and triggers the eruption simultaneously.

magma intruded into the middle crust (∼ 23–26 km depth) and crystallized olivine, clinopyroxene and plagioclase phenocrysts.

3. The Wulanhada intraplate monogenetic volcanism was triggered by the far-field effect of the Indian–Eurasian collision that caused partial melting of the mantle and repeated magma replenishment. The Wulanhada Volcanic Field may represent a snapshot of the transition from monogenetic volcanoes to composite volcanic eruptions.

Data availability. The data of Tables S1–S5 can be accessed from a reliable public data repository: https://doi.org/10.5281/zenodo.7188369 (Luo, 2022).

Supplement. The supplement related to this article is available online at: https://doi.org/10.5194/ejm-34-469-2022-supplement.

Author contributions. DL, TH, MW, JQ, DY and RP undertook the fieldwork and collected the rock samples. DL and RP carried out the EMPA. All authors discussed and interpreted the results. Acquisition of the financial support for the project was undertaken by TH. The manuscript was written by DL, MKR and TH with contributions from all co-authors: ZZ, XW and MS contributed to the Results and Discussion sections, and FH and RB contributed to the Abstract and Introduction of the paper.

Competing interests. The contact author has declared that none of the authors has any competing interests.

Disclaimer. Publisher's note: Copernicus Publications remains neutral with regard to jurisdictional claims in published maps and institutional affiliations.

Acknowledgements. We greatly appreciate the constructive comments and suggestions from Marco Brenna and the anonymous reviewer, which significantly improved our manuscript. We are also grateful to Elisabetta Rampone and Dewashish Upadhyay for their editorial handling. Thanks to Zongqi Zou and Zaicong Wang of the China University of Geosciences for assistance during the revision of the manuscript.

Financial support. This research has been supported by the National Key Research & Development Program of China (grant no. 2019YFA0708604-2); the Fundamental Research Funds for the Central Universities (grant nos. 2652018120 and 265QZ201901); the China University of Geosciences, Beijing (grant no. MSFGPMR201804); the Higher Education Discipline Innovation Project (grant no. B18048); an Alexander von Humboldt fellowship (grant no. 1207058); and the National Natural Science Foundation of China (grant no. 41922012).

Review statement. This paper was edited by Dewashish Upadhyay and reviewed by Marco Brenna and one anonymous referee.

References

Ablay, G. J., Carroll, M. R., Palmer, M. R., Martí, J., and Sparks, R. S. J.: Basanite–phonolite lineages of the Teide–Pico Viejo volcanic complex, Tenerife, Canary Islands, J. Petrol., 39, 905–936, https://doi.org/10.1093/petroj/39.5.905, 1998.

Armienti, P., Perinelli, C., and Putirka, K. D.: A new model to estimate deep-level magma ascent rates, with applications to Mt. Etna (Sicily, Italy), J. Petrol., 54, 795–813, https://doi.org/10.1093/petrology/egs085, 2013.

Bai, Z.-D., Wang, J.-M., Xu, G.-L., Liu, L., and Xu, D.-B.: Quaternary Volcano Cluster of Wulanhada, Right-back-banner, Chabaer, Inner Mongolia., Acta Petrol. Sin., 24, 2585–2594, 2008 (in Chinese with English abstract).

Boivin, P. and Thouret, J.-C.: The volcanic Chaîne des Puys: a unique collection of simple and compound monogenetic edifices, in: Landscapes and landforms of France, edited by: Fort, M. and Andre, M.-F., Springer, 81–91, https://doi.org/10.1007/978-94-007-7022-5_9, 2014.

Blondes, M. S., Reiners, P. W., Ducea, M. N., Singer, B. S., and Chesley, J.: Temporal–compositional trends over short and long time-scales in basalts of the Big Pine Volcanic Field, California, Earth Planet. Sc. Lett., 269, 140–154, 2008.

Brenna, M., Cronin, S. J., Smith, I. E., Sohn, Y. K., and Németh, K.: Mechanisms driving polymagmatic activity at a monogenetic volcano, Udo, Jeju Island, South Korea, Contrib. Mineral. Petr., 160, 931–950, https://doi.org/10.1007/s00410-010-0515-1, 2010.

Brenna, M., Cronin, S. J., Smith, I. E. M., Sohn, Y. K., and Maas, R.: Spatio-temporal evolution of a dispersed magmatic system and its implications for volcano growth, Jeju Island Volcanic Field, Korea, Lithos, 148, 337–352, https://doi.org/10.1016/j.lithos.2012.06.021, 2012.

Brenna, M., Cronin, S. J., Smith, I. E. M., Tollan, P. M. E., Scott, J. M., Prior, D. J., Bambery, K., and Ukstins, I. A.: Olivine xenocryst diffusion reveals rapid monogenetic basaltic magma ascent following complex storage at Pupuke Maar, Auckland Volcanic Field, New Zealand, Earth Planet. Sc. Lett., 499, 13–22, https://doi.org/10.1016/j.epsl.2018.07.015, 2018.

Brenna, M., Ubide, T., Nichols, A. R., Mollo, S., and Pontesilli, A.: Anatomy of Intraplate Monogenetic Alkaline Basaltic Magmatism: Clues From Magma, Crystals, and Glass, Crustal Magmat. Syst. Evol. Anat. Archit. Physico-Chemical Process., 79–103, https://doi.org/10.1002/9781119564485.ch4, 2021.

Bucchi, F., Lara, L. E., and Gutiérrez, F.: The Carrán–Los Venados volcanic field and its relationship with coeval and nearby polygenetic volcanism in an intra-arc setting, J. Volcanol. Geoth. Res., 308, 70–81, https://doi.org/10.1016/j.jvolgeores.2015.10.013, 2015.

Cañón-Tapia, E.: Reappraisal of the significance of volcanic fields, J. Volcanol. Geoth. Res., 310, 26–38, https://doi.org/10.1016/j.jvolgeores.2015.11.010, 2016.

Cañón-Tapia, E. and Walker, G. P. L.: Global aspects of volcanism: the perspectives of "plate tectonics" and "volcanic systems", Earth-Sci. Rev., 66, 163–182, https://doi.org/10.1016/j.earscirev.2003.11.001, 2004.

Chen, C., Liu, Y., Foley, S. F., Ducea, M. N., He, D., Hu, Z., Chen, W., and Zong, K.: Paleo-Asian oceanic slab under the North China craton revealed by carbonatites derived from subducted limestones, Geology, 44, 1039–1042, https://doi.org/10.1130/G38365.1, 2016.

Coote, A., Shane, P., Stirling, C., and Reid, M.: The origin of plagioclase phenocrysts in basalts from continental monogenetic volcanoes of the Kaikohe-Bay of Islands field, New Zealand: implications for magmatic assembly and ascent, Contrib. Mineral. Petr., 173, 1–19, 2018.

Coote, A., Shane, P., and Fu, B.: Olivine phenocryst origins and mantle magma sources for monogenetic basalt volcanoes in northern New Zealand from textural, geochemical and $\delta^{18}O$ isotope data, Lithos, 344, 232–246, https://doi.org/10.1016/j.lithos.2019.06.026, 2019.

Corazzato, C. and Tibaldi, A.: Fracture control on type, morphology and distribution of parasitic volcanic cones: an example from Mt. Etna, Italy, J. Volcanol. Geoth. Res., 158, 177–194, https://doi.org/10.1016/j.jvolgeores.2006.04.018, 2006.

Crossingham, T. J., Ubide, T., Vasconcelos, P. M., and Mallmann, G.: Parallel plumbing systems feeding a pair of coeval volcanoes in eastern Australia, J. Petrol., 59, 1035–1066, https://doi.org/10.1093/petrology/egy054, 2018.

Dasgupta, R., Hirschmann, M. M., and Withers, A. C.: Deep global cycling of carbon constrained by the solidus of anhydrous, carbonated eclogite under upper mantle conditions, Earth Planet. Sc. Lett., 227, 73–85, https://doi.org/10.1016/j.epsl.2004.08.004, 2004.

Dasgupta, R., Hirschmann, M. M., and Stalker, K.: Immiscible transition from carbonate-rich to silicate-rich melts in the 3 GPa melting interval of eclogite + CO_2 and genesis of silica-undersaturated ocean island lavas, J. Petrol., 47, 647–671, https://doi.org/10.1093/petrology/egi088, 2006.

Dasgupta, R., Hirschmann, M. M., and Smith, N. D.: Partial melting experiments of peridotite + CO_2 at 3 GPa and genesis of alkalic ocean island basalts, J. Petrol., 48, 2093–2124, https://doi.org/10.1093/petrology/egm053, 2007.

Dasgupta, R., Hirschmann, M. M., McDonough, W. F., Spiegelman, M., and Withers, A. C.: Trace element partitioning between garnet lherzolite and carbonatite at 6.6 and 8.6 GPa with applications to the geochemistry of the mantle and of mantle-derived melts, Chem. Geol., 262, 57–77, https://doi.org/10.1016/j.chemgeo.2009.02.004, 2009.

Dasgupta, R., Mallik, A., Tsuno, K., Withers, A. C., Hirth, G., and Hirschmann, M. M.: Carbon-dioxide-rich silicate melt in the Earth's upper mantle, Nature, 493, 211–215, https://doi.org/10.1038/nature11731, 2013.

Davis, F. A., Hirschmann, M. M., and Humayun, M.: The composition of the incipient partial melt of garnet peridotite at 3 GPa and the origin of OIB, Earth Planet. Sc. Lett., 308, 380–390, https://doi.org/10.1016/j.epsl.2011.06.008, 2011.

Devine, J. D., Rutherford, M. J., Norton, G. E., and Young, S. R.: Magma Storage Region Processes Inferred from Geochemistry of Fe–Ti Oxides in Andesitic Magma, Soufrière Hills Volcano, Montserrat, W.I., J. Petrol., 44, 1375–1400, https://doi.org/10.1093/petrology/44.8.1375, 2003.

Dvir, O. and Kessel, R.: The effect of CO_2 on the water-saturated solidus of K-poor peridotite between 4 and 6 GPa, Geochim. Cosmochim. Ac., 206, 184–200, https://doi.org/10.1016/j.gca.2017.02.028, 2017.

Elardo, S. M. and Shearer Jr., C. K.: Magma chamber dynamics recorded by oscillatory zoning in pyroxene and olivine phenocrysts in basaltic lunar meteorite Northwest Africa 032, Am. Mineral., 99, 355–368, https://doi.org/10.2138/am.2014.4552, 2014.

Elazar, O., Frost, D., Navon, O., and Kessel, R.: Melting of H_2O and CO_2-bearing eclogite at 4–6 GPa and 900–1200 °C: implications for the generation of diamond-forming fluids, Geochim. Cosmochim. Ac., 255, 69–87, https://doi.org/10.1016/j.gca.2019.03.025, 2019.

Fan, Q.-C., Chen, S.-S., Zhao, Y.-W., Zou, H.-B., Li, N., and Sui, J.-L.: Petrogenesis and evolution of Quaternary basaltic rocks

from the Wulanhada area, North China, Lithos, 206, 289–302, https://doi.org/10.1016/j.lithos.2014.08.007, 2014.

Foley, S. F., Yaxley, G. M., Rosenthal, A., Buhre, S., Kiseeva, E. S., Rapp, R. P., and Jacob, D. E.: The composition of near-solidus melts of peridotite in the presence of CO_2 and H_2O between 40 and 60 kbar, Lithos, 112, 274–283, https://doi.org/10.1016/j.lithos.2009.03.020, 2009.

Gale, A., Dalton, C. A., Langmuir, C. H., Su, Y., and Schilling, J.-G.: The mean composition of ocean ridge basalts, Geochem. Geophys. Geosy., 14, 489–518, https://doi.org/10.1029/2012GC004334, 2013.

Gamble, J. A., Price, R. C., Smith, I. E., McIntosh, W. C., and Dunbar, N. W.: $^{40}Ar/^{39}Ar$ geochronology of magmatic activity, magma flux and hazards at Ruapehu volcano, Taupo Volcanic Zone, New Zealand, J. Volcanol. Geoth. Res., 120, 271–287, https://doi.org/10.1016/S0377-0273(02)00407-9, 2003.

Gerbode, C. and Dasgupta, R.: Carbonate-fluxed melting of MORB-like pyroxenite at 2.9 GPa and genesis of HIMU ocean island basalts, J. Petrol., 51, 2067–2088, https://doi.org/10.1093/petrology/egq049, 2010.

Gernon, T. M., Upton, B. G. J., Ugra, R., Yücel, C., Taylor, R. N., and Elliott, H.: Complex subvolcanic magma plumbing system of an alkali basaltic maar-diatreme volcano (Elie Ness, Fife, Scotland), Lithos, 264, 70–85, https://doi.org/10.1016/j.lithos.2016.08.001, 2016.

Ghosh, S., Litasov, K., and Ohtani, E.: Phase relations and melting of carbonated peridotite between 10 and 20 GPa: a proxy for alkali-and CO_2-rich silicate melts in the deep mantle, Contrib. Mineral. Petr., 167, 1–23, https://doi.org/10.1007/s00410-014-0964-z, 2014.

Ginibre, C., Kronz, A., and Wörner, G.: High-resolution quantitative imaging of plagioclase composition using accumulated backscattered electron images: new constraints on oscillatory zoning, Contrib. Mineral. Petr., 142, 436–448, https://doi.org/10.1007/s004100100298, 2002.

Hammouda, T.: High-pressure melting of carbonated eclogite and experimental constraints on carbon recycling and storage in the mantle, Earth Planet. Sc. Lett., 214, 357–368, https://doi.org/10.1016/S0012-821X(03)00361-3, 2003.

Hasebe, N., Fukutani, A., Sudo, M., and Tagami, T.: Transition of eruptive style in an arc–arc collision zone: K–Ar dating of Quaternary monogenetic and polygenetic volcanoes in the Higashi-Izu region, Izu peninsula, Japan, Bull. Volcanol., 63, 377–386, https://doi.org/10.1007/s004450100158, 2001.

Herzberg, C.: Petrology and thermal structure of the Hawaiian plume from Mauna Kea volcano, Nature, 444, 605–609, https://doi.org/10.1038/nature05254, 2006.

Herzberg, C.: Identification of source lithology in the Hawaiian and Canary Islands: Implications for origins, J. Petrol., 52, 113–146, https://doi.org/10.1093/petrology/egq075, 2011.

Hildreth, W.: Quaternary magmatism in the Cascades: Geologic perspectives, edited by: Handley, J. W., US Geological Survey, 125 pp., http://pubs.usgs.gov/pp/pp1744/ (last access: 12 October 2022), 2007.

Hirose, K.: Partial melt compositions of carbonated peridotite at 3 GPa and role of CO_2 in alkali-basalt magma generation, Geophys. Res. Lett., 24, 2837–2840, https://doi.org/10.1029/97GL02956, 1997.

Hirose, K. and Kushiro, I.: Partial melting of dry peridotites at high pressures: determination of compositions of melts segregated from peridotite using aggregates of diamond, Earth Planet. Sc. Lett., 114, 477–489, https://doi.org/10.1016/0012-821X(93)90077-M, 1993.

Hirschmann, M. M., Kogiso, T., Baker, M. B., and Stolper, E. M.: Alkalic magmas generated by partial melting of garnet pyroxenite, Geology, 31, 481–484, https://doi.org/10.1130/0091-7613(2003)031<0481:AMGBPM>2.0.CO;2, 2003.

Hoernle, K., Tilton, G., Le Bas, M. J., Duggen, S., and Garbe-Schönberg, D.: Geochemistry of oceanic carbonatites compared with continental carbonatites: mantle recycling of oceanic crustal carbonate, Contrib. Mineral. Petr., 142, 520–542, https://doi.org/10.1007/s004100100308, 2002.

Hofmann, A. W., Jochum, K. P., Seufert, M., and White, W. M.: Nb and Pb in oceanic basalts: new constraints on mantle evolution, Earth Planet. Sc. Lett., 79, 33–45, https://doi.org/10.1016/0012-821X(86)90038-5, 1986.

Howarth, G. H. and Taylor, L. A.: Multi-stage kimberlite evolution tracked in zoned olivine from the Benfontein sill, South Africa, Lithos, 262, 384–397, https://doi.org/10.1016/j.lithos.2016.07.028, 2016.

Huang, J. and Zhao, D.: High-resolution mantle tomography of China and surrounding regions, J. Geophys. Res.-Sol. Ea., 111, B09305, https://doi.org/10.1029/2005JB004066, 2006.

Irvine, T. N. and Baragar, W.: A Guide to the Chemical Classification of the Common Volcanic Rocks, Can. J. Earth Sci., 8, 523–548, https://doi.org/10.1139/e71-055, 1971.

Kahl, M., Chakraborty, S., Costa, F., and Pompilio, M.: Dynamic plumbing system beneath volcanoes revealed by kinetic modeling, and the connection to monitoring data: An example from Mt. Etna, Earth Planet. Sc. Lett., 308, 11–22, https://doi.org/10.1016/j.epsl.2011.05.008, 2011.

Kiseeva, E. S., Yaxley, G. M., Hermann, J., Litasov, K. D., Rosenthal, A., and Kamenetsky, V. S.: An experimental study of carbonated eclogite at 3.5–5.5 GPa – implications for silicate and carbonate metasomatism in the cratonic mantle, J. Petrol., 53, 727–759, https://doi.org/10.1093/petrology/egr078, 2012.

Klemme, S., Blundy, J. D., and Wood, B. J.: Experimental constraints on major and trace element partitioning during partial melting of eclogite, Geochim. Cosmochim. Ac., 66, 3109–3123, https://doi.org/10.1016/S0016-7037(02)00859-1, 2002.

Kogiso, T., Hirschmann, M. M., and Frost, D. J.: High-pressure partial melting of garnet pyroxenite: possible mafic lithologies in the source of ocean island basalts, Earth Planet. Sc. Lett., 216, 603–617, https://doi.org/10.1016/S0012-821X(03)00538-7, 2003.

Kogiso, T., Hirschmann, M. M., and Reiners, P. W.: Length scales of mantle heterogeneities and their relationship to ocean island basalt geochemistry, Geochim. Cosmochim. Ac., 68, 345–360, https://doi.org/10.1016/S0016-7037(03)00419-8, 2004.

Lambart, S., Laporte, D., and Schiano, P.: Markers of the pyroxenite contribution in the major-element compositions of oceanic basalts: Review of the experimental constraints, Lithos, 160, 14–36, https://doi.org/10.1016/j.lithos.2012.11.018, 2013.

Le Bas, M. L., Le Maitre, R. W., Streckeisen, A., Zanettin, B., and IUGS Subcommission on the Systematics of Igneous Rocks: A chemical classification of volcanic rocks based on the total alkali-silica diagram, J. Petrol., 27, 745–750, https://doi.org/10.1093/petrology/27.3.745, 1986.

Le Roux, V., Lee, C.-T., and Turner, S. J.: Zn/Fe systematics in mafic and ultramafic systems: Implications for detecting major element heterogeneities in the Earth's mantle, Geochim. Cosmochim. Ac., 74, 2779–2796, https://doi.org/10.1016/j.gca.2010.02.004, 2010.

Li, J.-Y.: Permian geodynamic setting of Northeast China and adjacent regions: closure of the Paleo-Asian Ocean and subduction of the Paleo-Pacific Plate, J. Asian Earth Sci., 26, 207–224, https://doi.org/10.1016/j.jseaes.2005.09.001, 2006.

Lindsay, J. M., Leonard, G. S., Smid, E. R., and Hayward, B. W.: Age of the Auckland Volcanic Field: a review of existing data, New Zeal. J. Geol. Geop., 54, 379–401, https://doi.org/10.1080/00288306.2011.595805, 2011.

Litasov, K. D., Shatskiy, A. F., and Pokhilenko, N. P.: Phase relations and melting in the systems of peridotite-H_2O-CO_2 and eclogite-H_2O-CO_2 at pressures up to 27 GPa, Dokl. Earth Sc., 437, 498–502, https://doi.org/10.1134/S1028334X11040143, 2011.

Liu, M., Cui, X., and Liu, F.: Cenozoic rifting and volcanism in eastern China: a mantle dynamic link to the Indo–Asian collision?, Tectonophysics, 393, 29–42, https://doi.org/10.1016/j.tecto.2004.07.029, 2004.

Liu, R. X., Chen, W. J., and Sun, J. Z.: The K-Ar age and tectonic environment of Cenozoic volcanic rock in China, The Age and Geochemistry of Cenozoic Volcanic Rock in China, edited by: Liu, R., Seismic Press, Beijing, 1–43, 1992.

Liu, X., Zhao, D., Li, S., and Wei, W.: Age of the subducting Pacific slab beneath East Asia and its geodynamic implications, Earth Planet. Sc. Lett., 464, 166–174, https://doi.org/10.1016/j.epsl.2017.02.024, 2017.

Longpré, M.-A., Klügel, A., Diehl, A., and Stix, J.: Mixing in mantle magma reservoirs prior to and during the 2011–2012 eruption at El Hierro, Canary Islands, Geology, 42, 315–318, https://doi.org/10.1130/G35165.1, 2014.

Lu, J.-C., Wei, X.-Y., Cao, X.-D., and Zhang, R.-L.: Research on CO_2 gas pool-geological conditions in Shangdu area, Inner Mongolia, Northwest. Geol., 35, 122–134, 2002 (in Chinese with English abstract).

Luo, D.: Supplementary information of Tables S1–S5, Zenodo [data set], https://doi.org/10.5281/zenodo.7188369, 2022.

Lynch, D. J., Musselman, T. E., Gutmann, J. T., and Patchett, P. J.: Isotopic evidence for the origin of Cenozoic volcanic rocks in the Pinacate volcanic field, northwestern Mexico, Lithos, 29, 295–302, https://doi.org/10.1016/0024-4937(93)90023-6, 1993.

Ma, X.: Lithospheric dynamics atlas of China, China Cartogr., Publ. House Beijing, 1989.

Martin, U. and Németh, K.: How Strombolian is a "Strombolian" scoria cone? Some irregularities in scoria cone architecture from the Transmexican Volcanic Belt, near Volcán Ceboruco,(Mexico) and Al Haruj (Libya), J. Volcanol. Geoth. Res., 155, 104–118, https://doi.org/10.1016/j.jvolgeores.2006.02.012, 2006.

Maruyama, S.: Pacific-type orogeny revisited: Miyashiro-type orogeny proposed, Isl. Arc, 6, 91–120, https://doi.org/10.1111/j.1440-1738.1997.tb00042.x, 1997.

McGee, L. E. and Smith, I. E.: Interpreting chemical compositions of small scale basaltic systems: a review, J. Volcanol. Geoth. Res., 325, 45–60, https://doi.org/10.1016/j.jvolgeores.2016.06.007, 2016.

McGee, L. E., Beier, C., Smith, I. E., and Turner, S. P.: Dynamics of melting beneath a small-scale basaltic system: a U-Th–Ra study from Rangitoto volcano, Auckland volcanic field, New Zealand, Contrib. Mineral. Petr., 162, 547–563, https://doi.org/10.1007/s00410-011-0611-x, 2011.

McGee, L. E., Smith, I. E., Millet, M.-A., Handley, H. K., and Lindsay, J. M.: Asthenospheric control of melting processes in a monogenetic basaltic system: a case study of the Auckland Volcanic Field, New Zealand, J. Petrol., 54, 2125–2153, https://doi.org/10.1093/petrology/egt043, 2013.

McLeod, O. E., Brenna, M., Briggs, R. M., and Pittari, A.: Slab tear as a cause of coeval arc-intraplate volcanism in the Alexandra Volcanic Group, New Zealand, Lithos, 408, 106564, https://doi.org/10.1016/j.lithos.2021.106564, 2022.

Morimoto, N.: Nomenclature of pyroxenes, Mineral. Petrol., 39, 55–76, https://doi.org/10.1007/BF01226262, 1988.

Muffler, L. J. P., Clynne, M. A., Calvert, A. T., and Champion, D. E.: Diverse, discrete, mantle-derived batches of basalt erupted along a short normal fault zone: The Poison Lake chain, southernmost Cascades, Bulletin, 123, 2177–2200, 2011.

Neave, D. A. and Putirka, K. D.: A new clinopyroxene-liquid barometer, and implications for magma storage pressures under Icelandic rift zones, Am. Mineral., 102, 777–794, https://doi.org/10.2138/am-2017-5968, 2017.

Neill, O. K., Larsen, J. F., Izbekov, P. E., and Nye, C. J.: Pre-eruptive magma mixing and crystal transfer revealed by phenocryst and microlite compositions in basaltic andesite from the 2008 eruption of Kasatochi Island volcano, Am. Mineral., 100, 722–737, https://doi.org/10.2138/am-2015-4967, 2015.

Németh, K. and Kereszturi, G.: Monogenetic volcanism: personal views and discussion, Int. J. Earth Sci., 104, 2131–2146, https://doi.org/10.1007/s00531-015-1243-6, 2015.

Niu, Y. L.: Generation and evolution of basaltic magmas: some basic concepts and a new view on the origin of Mesozoic–Cenozoic basaltic volcanism in eastern China, Geol. J. China Univ., 11, 9–46, 2005.

Niu, Y. L. and O'Hara, M. J.: Origin of ocean island basalts: A new perspective from petrology, geochemistry, and mineral physics considerations, J. Geophys. Res.-Sol. Ea., 108, 2209, https://doi.org/10.1029/2002JB002048, 2003.

Peccerillo, A. and Taylor, S. R.: Geochemistry of Eocene calc-alkaline volcanic rocks from the Kastamonu area, northern Turkey, Contrib. Mineral. Petr., 58, 63–81, https://doi.org/10.1007/BF00384745, 1976.

Perinelli, C., Mollo, S., Gaeta, M., De Cristofaro, S. P., Palladino, D. M., Armienti, P., Scarlato, P., and Putirka, K. D.: An improved clinopyroxene-based hygrometer for Etnean magmas and implications for eruption triggering mechanisms, Am. Mineral., 101, 2774–2777, https://doi.org/10.2138/am-2016-5916, 2016.

Pertermann, M. and Hirschmann, M. M.: Anhydrous partial melting experiments on MORB-like eclogite: phase relations, phase compositions and mineral–melt partitioning of major elements at 2–3 GPa, J. Petrol., 44, 2173–2201, https://doi.org/10.1093/petrology/egg074, 2003.

Pertermann, M., Hirschmann, M. M., Hametner, K., Günther, D., and Schmidt, M. W.: Experimental determination of trace element partitioning between garnet and silica-rich liquid during anhydrous partial melting of MORB-

like eclogite, Geochem. Geophys. Geosy., 5, Q05A01, https://doi.org/10.1029/2003GC000638, 2004.

Pilet, S., Baker, M. B., and Stolper, E. M.: Metasomatized lithosphere and the origin of alkaline lavas, Science, 320, 916–919, https://doi.org/10.1126/science.1156563, 2008.

Pintér, Z., Foley, S. F., Yaxley, G. M., Rosenthal, A., Rapp, R. P., Lanati, A. W., and Rushmer, T.: Experimental investigation of the composition of incipient melts in upper mantle peridotites in the presence of CO_2 and H_2O, Lithos, 396, 106224, https://doi.org/10.1016/j.lithos.2021.106224, 2021.

Pontesilli, A., Brenna, M., Ubide, T., Mollo, S., Masotta, M., Caulfield, J., Le Roux, P., Nazzari, M., Scott, J. M., and Scarlato, P.: Intraplate basalt alkalinity modulated by a lithospheric mantle filter at the Dunedin Volcano (New Zealand), J. Petrol., 62, egab062, https://doi.org/10.1093/petrology/egab062, 2021.

Putirka, K.: Clinopyroxene + liquid equilibria to 100 kbar and 2450 K, Contrib. Mineral. Petr., 135, 151–163, https://doi.org/10.1007/s004100050503, 1999.

Putirka, K. D.: Thermometers and barometers for volcanic systems, Rev. Mineral. Geochem., 69, 61–120, https://doi.org/10.2138/rmg.2008.69.3, 2008.

Re, G., Palin, J. M., White, J. D. L., and Parolari, M.: Unravelling the magmatic system beneath a monogenetic volcanic complex (Jagged Rocks Complex, Hopi Buttes, AZ, USA), Contrib. Mineral. Petr., 172, 1–27, https://doi.org/10.1007/s00410-017-1410-9, 2017.

Roeder, P. L. and Emslie, R.: Olivine-liquid equilibrium, Contrib. Mineral. Petr., 29, 275–289, https://doi.org/10.1007/BF00371276, 1970.

Rudnick, R. L., McDonough, W. F., and Chappell, B. W.: Carbonatite metasomatism in the northern Tanzanian mantle: petrographic and geochemical characteristics, Earth Planet. Sc. Lett., 114, 463–475, https://doi.org/10.1016/0012-821X(93)90076-L, 1993.

Sakuyama, T., Tian, W., Kimura, J.-I., Fukao, Y., Hirahara, Y., Takahashi, T., Senda, R., Chang, Q., Miyazaki, T., and Obayashi, M.: Melting of dehydrated oceanic crust from the stagnant slab and of the hydrated mantle transition zone: Constraints from Cenozoic alkaline basalts in eastern China, Chem. Geol., 359, 32–48, https://doi.org/10.1016/j.chemgeo.2013.09.012, 2013.

Sengor, A. M. C. and Natalin, B. A.: Paleotectonics of Asia: fragments of a synthesis, The tectonic evolution of Asia, edited by: Yin, A. and Harrison, T. M., Cambridge University Press, 486–640, 1996.

Shaw, D. M.: Trace element fractionation during anatexis, Geochim. Cosmochim. Ac., 34, 237–243, https://doi.org/10.1016/0016-7037(70)90009-8, 1970.

Shea, J. J. and Foley, S. F.: Evidence for a carbonatite-influenced source assemblage for intraplate basalts from the Buckland Volcanic Province, Queensland, Australia, Minerals, 9, 546, https://doi.org/10.3390/min9090546, 2019.

Shore, M. and Fowler, A. D.: Oscillatory zoning in minerals; a common phenomenon, Can. Mineral., 34, 1111–1126, 1996.

Smith, I. E. M. and Németh, K.: Source to surface model of monogenetic volcanism: a critical review, Geol. Soc. Lond. Spec. Publ., 446, 1–28, https://doi.org/10.1144/SP446.14, 2017.

Sobolev, A. V., Hofmann, A. W., Sobolev, S. V., and Nikogosian, I. K.: An olivine-free mantle source of Hawaiian shield basalts, Nature, 434, 590–597, https://doi.org/10.1038/nature03411, 2005.

Sobolev, A. V., Hofmann, A. W., Kuzmin, D. V., Yaxley, G. M., Arndt, N. T., Chung, S.-L., Danyushevsky, L. V., Elliott, T., Frey, F. A., and Garcia, M. O.: The amount of recycled crust in sources of mantle-derived melts, Science, 316, 412–417, 2007.

Spandler, C., Yaxley, G., Green, D. H., and Rosenthal, A.: Phase relations and melting of anhydrous K-bearing eclogite from 1200 to 1600 °C and 3 to 5 GPa, J. Petrol., 49, 771–795, https://doi.org/10.1093/petrology/egm039, 2008.

Sparks, R. S. J., Annen, C., Blundy, J. D., Cashman, K. V., Rust, A. C., and Jackson, M. D.: Formation and dynamics of magma reservoirs, Philos. T. R. Soc. A, 377, 20180019, https://doi.org/10.1098/rsta.2018.0019, 2018.

Streck, M. J.: Mineral textures and zoning as evidence for open system processes, Rev. Mineral. Geochem., 69, 595–622, https://doi.org/10.2138/rmg.2008.69.15, 2008.

Sun, P., Niu, Y., Guo, P., Cui, H., Ye, L., and Liu, J.: The evolution and ascent paths of mantle xenolith-bearing magma: Observations and insights from Cenozoic basalts in Southeast China, Lithos, 310, 171–181, https://doi.org/10.1016/j.lithos.2018.04.015, 2018.

Sun, S. S. and McDonough, W. F.: Chemical and isotopic systematics of ocean basalts: Implications for mantle composition and processes, in Magmatism in the Ocean Basins, Geol. Soc. Lond. Spec. Publ., 423, 13–345, 1989.

Sun, Y., Teng, F.-Z., and Pang, K.-N.: The presence of paleo-Pacific slab beneath northwest North China Craton hinted by low-δ^{26}Mg basalts at Wulanhada, Lithos, 386, 106009, https://doi.org/10.1016/j.lithos.2021.106009, 2021.

Takada, A.: The influence of regional stress and magmatic input on styles of monogenetic and polygenetic volcanism, J. Geophys. Res.-Sol. Ea., 99, 13563–13573, https://doi.org/10.1029/94JB00494, 1994.

Takahashi, E. and Kushiro, I.: Melting of a dry peridotite at high pressures and basalt magma genesis, Am. Mineral., 68, 859–879, 1983.

Takahashi, E. and Scarfe, C. M.: Melting of peridotite to 14 GPa and the genesis of komatiite, Nature, 315, 566–568, https://doi.org/10.1038/315566a0, 1985.

Takahashi, E., Shimazaki, T., Tsuzaki, Y., and Yoshida, H.: Melting study of a peridotite KLB-1 to 6.5 GPa, and the origin of basaltic magmas, Philos. T. Roy. Soc. A, 342, 105–120, https://doi.org/10.1098/rsta.1993.0008, 1993.

Tanaka, K. L., Shoemaker, E. M., Ulrich, G. E., and Wolfe, E. W.: Migration of volcanism in the San Francisco volcanic field, Arizona, Geol. Soc. Am. Bull., 97, 129–141, https://doi.org/10.1130/0016-7606(1986)97<129:MOVITS>2.0.CO;2, 1986.

Tchamabé, B. C., Kereszturi, G., Németh, K., and Carrasco-Núñez, G.: How polygenetic are monogenetic volcanoes: case studies of some complex maar-diatreme volcanoes, Updat. Volcanol.-Volcano Model. Volcano Geol., 13, 355–389, 2016.

Teng, F.-Z., Li, W.-Y., Ke, S., Marty, B., Dauphas, N., Huang, S., Wu, F.-Y., and Pourmand, A.: Magnesium isotopic composition of the Earth and chondrites, Geochim. Cosmochim. Ac., 74, 4150–4166, https://doi.org/10.1016/j.gca.2010.04.019, 2010.

Thomson, A. R., Walter, M. J., Kohn, S. C., and Brooker, R. A.: Slab melting as a barrier to deep carbon subduction, Nature, 529, 76–79, https://doi.org/10.1038/nature16174, 2016.

Ubide, T. and Kamber, B. S.: Volcanic crystals as time capsules of eruption history, Nat. Commun., 9, 1–12, https://doi.org/10.1038/s41467-017-02274-w, 2018.

Ubide, T., Galé, C., Larrea, P., Arranz, E., and Lago, M.: Antecrysts and their effect on rock compositions: the Cretaceous lamprophyre suite in the Catalonian Coastal Ranges (NE Spain), Lithos, 206, 214–233, https://doi.org/10.1016/j.lithos.2014.07.029, 2014.

Valentine, G. A. and Gregg, T. K. P.: Continental basaltic volcanoes – processes and problems, J. Volcanol. Geoth. Res., 177, 857–873, https://doi.org/10.1016/j.jvolgeores.2008.01.050, 2008.

Valentine, G. A., Perry, F. V., Krier, D., Keating, G. N., Kelley, R. E., and Cogbill, A. H.: Small-volume basaltic volcanoes: Eruptive products and processes, and posteruptive geomorphic evolution in Crater Flat (Pleistocene), southern Nevada, Geol. Soc. Am. Bull., 118, 1313–1330, https://doi.org/10.1130/B25956.1, 2006.

Walker, G. P.: Basaltic-volcano systems, Geol. Soc. Lond. Spec. Publ., 76, 3–38, https://doi.org/10.1144/GSL.SP.1993.076.01.01, 1993.

Walker, J. A., Singer, B. S., Jicha, B. R., Cameron, B. I., Carr, M. J., and Olney, J. L.: Monogenetic, behind-the-front volcanism in southeastern Guatemala and western El Salvador: $^{40}Ar/^{39}Ar$ ages and tectonic implications, Lithos, 123, 243–253, https://doi.org/10.1016/j.lithos.2010.09.016, 2011.

Walter, M. J.: Melting of garnet peridotite and the origin of komatiite and depleted lithosphere, J. Petrol., 39, 29–60, https://doi.org/10.1093/petroj/39.1.29, 1998.

Wang, Z.-Z. and Liu, S.-A.: Evolution of intraplate alkaline to tholeiitic basalts via interaction between carbonated melt and lithospheric mantle, J. Petrol., 62, egab025, https://doi.org/10.1093/petrology/egab025, 2021.

Watanabe, S., Widom, E., Ui, T., Miyaji, N., and Roberts, A. M.: The evolution of a chemically zoned magma chamber: The 1707 eruption of Fuji volcano, Japan, J. Volcanol. Geoth. Res., 152, 1–19, https://doi.org/10.1016/j.jvolgeores.2005.08.002, 2006.

Wei, H., Wang, Y., Jin, J., Gao, L., Yun, S.-H., and Jin, B.: Timescale and evolution of the intracontinental Tianchi volcanic shield and ignimbrite-forming eruption, Changbaishan, Northeast China, Lithos, 96, 315–324, https://doi.org/10.1016/j.lithos.2006.10.004, 2007.

Wei, W., Xu, J., Zhao, D., and Shi, Y.: East Asia mantle tomography: New insight into plate subduction and intraplate volcanism, J. Asian Earth Sci., 60, 88–103, https://doi.org/10.1016/j.jseaes.2012.08.001, 2012.

Wilson, L. and Head III, J. W.: Nature of local magma storage zones and geometry of conduit systems below basaltic eruption sites: Pu'u'O'o, Kilauea East Rift, Hawaii, example, J. Geophys. Res.-Sol. Ea., 93, 14785–14792, https://doi.org/10.1029/JB093iB12p14785, 1988.

Workman, R. K. and Hart, S. R.: Major and trace element composition of the depleted MORB mantle (DMM), Earth Planet. Sc. Lett., 231, 53–72, https://doi.org/10.1016/j.epsl.2004.12.005, 2005.

Wu, F.-Y., Lin, J.-Q., Wilde, S. A., and Yang, J.-H.: Nature and significance of the Early Cretaceous giant igneous event in eastern China, Earth Planet. Sc. Lett., 233, 103–119, https://doi.org/10.1016/j.epsl.2005.02.019, 2005.

Xu, W.-L., Pei, F.-P., Wang, F., Meng, E., Ji, W.-Q., Yang, D.-B., and Wang, W.: Spatial–temporal relationships of Mesozoic volcanic rocks in NE China: constraints on tectonic overprinting and transformations between multiple tectonic regimes, J. Asian Earth Sci., 74, 167–193, https://doi.org/10.1016/j.jseaes.2013.04.003, 2013.

Xu, Y.-G., Ma, J.-L., Frey, F. A., Feigenson, M. D., and Liu, J.-F.: Role of lithosphere–asthenosphere interaction in the genesis of Quaternary alkali and tholeiitic basalts from Datong, western North China Craton, Chem. Geol., 224, 247–271, https://doi.org/10.1016/j.chemgeo.2005.08.004, 2005.

Yang, J.-H., Wu, F.-Y., Shao, J.-A., Wilde, S. A., Xie, L.-W., and Liu, X.-M.: Constraints on the timing of uplift of the Yanshan Fold and Thrust Belt, North China, Earth Planet. Sc. Lett., 246, 336–352, https://doi.org/10.1016/j.epsl.2006.04.029, 2006.

Yang, Z.-F., Li, J., Jiang, Q.-B., Xu, F., Guo, S.-Y., Li, Y., and Zhang, J.: Using major element logratios to recognize compositional patterns of basalt: Implications for source lithological and compositional heterogeneities, J. Geophys. Res.-Sol. Ea., 124, 3458–3490, https://doi.org/10.1029/2018JB016145, 2019.

Yaxley, G. M. and Green, D. H.: Reactions between eclogite and peridotite: mantle refertilisation by subduction of oceanic crust, Schweiz. Miner. Petrog., 78, 243–255, 1998.

Zellmer, G. F. and Annen, C.: An introduction to magma dynamics, Geol. Soc. Lond. Spec. Publ., 304, 1, https://doi.org/10.1144/SP304.1, 2008.

Zhang, G.-L., Chen, L.-H., Jackson, M. G., and Hofmann, A. W.: Evolution of carbonated melt to alkali basalt in the South China Sea, Nat. Geosci., 10, 229–235, https://doi.org/10.1038/ngeo2877, 2017.

Zhang, S.-H., Zhao, Y., Liu, X.-C., Liu, D.-Y., Chen, F., Xie, L.-W., and Chen, H.-H.: Late Paleozoic to Early Mesozoic mafic–ultramafic complexes from the northern North China Block: constraints on the composition and evolution of the lithospheric mantle, Lithos, 110, 229–246, https://doi.org/10.1016/j.lithos.2009.01.008, 2009.

Zhang, Y., Yuan, C., Sun, M., Huang, Z., Narantsetseg, T., Ren, Z., Li, P., and Zhang, Q.: Contrasting compositions between phenocrystic and xenocrystic olivines in the Cenozoic basalts from central Mongolia: Constraints on source lithology and regional uplift, Am. Mineral., 106, 251–264, https://doi.org/10.2138/am-2020-7431, 2021.

Zhao, G., Wilde, S. A., Cawood, P. A., and Sun, M.: Archean blocks and their boundaries in the North China Craton: lithological, geochemical, structural and P–T path constraints and tectonic evolution, Precambrian Res., 107, 45–73, https://doi.org/10.1016/S0301-9268(00)00154-6, 2001.

Zhao, Y.-W., Fan, Q.-C., Zou, H.-B., and Li, N.: Tectonic controls of Late Cenozoic monogenetic intraplate volcanism at the Wulanhada volcanic field, Northern China, J. Volcanol. Geoth. Res., 383, 16–27, https://doi.org/10.1016/j.jvolgeores.2018.01.022, 2019.

Zhou, X. and Armstrong, R. L.: Cenozoic volcanic rocks of eastern China – secular and geographic trends in chemistry and strontium isotopic composition, Earth Planet. Sc. Lett., 58, 301–329, https://doi.org/10.1016/0012-821X(82)90083-8, 1982.

Zou, Z., Wang, Z., Foley, S., Xu, R., Geng, X., Liu, Y.-N., Liu, Y., and Hu, Z.: Origin of low-MgO primitive intraplate alkaline basalts from partial melting of carbonate-bearing eclogite sources, Geochim. Cosmochim. Ac., 324, 240–261, https://doi.org/10.1016/j.gca.2022.02.022, 2022.